

Integrative Bayesian models using Post-selective Inference: a case study in Radiogenomics

Snigdha Panigrahi^{*1}, Shariq Mohammed^{2,3}, Arvind Rao^{2,3,4,5}, and
Veerabhadran Baladandayuthapani^{†2,3}

¹Department of Statistics, University of Michigan.

²Department of Biostatistics, University of Michigan.

³Department of Computational Medicine and Bioinformatics,, University of Michigan.

⁴Department of Biomedical Engineering, University of Michigan.

⁵Department of Radiation Oncology, University of Michigan.

Abstract

Identifying direct links between genomic pathways and clinical endpoints for highly fatal diseases such as cancer is a formidable task. By selecting statistically relevant associations between a wealth of intermediary variables such as imaging and genomic measurements, integrative analyses can potentially results in sharper clinical models with interpretable parameters, in terms of their mechanisms. Estimates of uncertainty in the resulting models are however unreliable unless inference accounts for the preceding steps of selection. In this article, we develop selection-aware Bayesian methods which are: (i) amenable to a flexible class of integrative Bayesian models post a selection of promising variables via ℓ_1 -regularized algorithms; (ii) enjoy computational

^{*}psnigdha@umich.edu

[†]veerab@umich.edu

efficiency due to a focus on sharp models with meaning; (iii) strike a crucial tradeoff between the quality of model selection and inferential power. Central to our selection-aware workflow, a conditional likelihood constructed with a reparameterization map is deployed for obtaining uncertainty estimates in integrative models. Investigating the potential of our methods in a radiogenomic analysis, we successfully recover several important gene pathways and calibrate uncertainties for their associations with patient survival times.

1 Introduction

Our methodology in the paper is motivated by a radiogenomic analysis in low-grade gliomas (LGG), a type of brain cancers. Briefly, a radiogenomic investigation refers to a task of assessing associations between imaging outcomes obtained from radiological imaging modalities, e.g. magnetic resonance imaging (MRI) with corresponding molecular and genomic markers. Specifically, the imaging outcomes play the role of intermediary variables in radiogenomic analyses (Zhang et al., 2019). These associations are then utilized to establish important biological links with patients' outcomes to understand the development and progression of diseases (Mazurowski, 2015; Gevaert et al., 2017).

Genomic instability and mutations are established hallmarks of cancer (Negrini et al., 2010; Tubbs and Nussenzweig, 2017). Nonetheless models attempting to link genes directly with clinical endpoints often prove to be quite limiting in terms of prognostic abilities, failing to explain much variability in the clinical outcomes (Mazurowski, 2015; Nicolasjilwan et al., 2015; Hu et al., 2017). The impediments to model efficacy in radiogenomic analyses are primarily attributed to a high dimensional set of sparse genomic variables sharing complex correlation structures, compounded with (relatively) small sample sizes. Sparsity of signal variables in these dimensions thus leads to regression problems with very low signal-to-noise ratios. Instead, sharp integrative models recovering the support of signal variables are usually defined post a selection of statistically relevant associations between an initial set of genomic variables, and the imaging variables and clinical outcomes. Exploiting in particular the associations between the imaging information for tumors with genomic measurements

pins down these genomic drivers in clinical models with better accuracy and interpretation (see Guo et al., 2015; Bakas et al., 2017).

From an inferential standpoint, integrative models harnessing promising associations between different modalities of information pose several serious challenges in high dimensional regimes. The radiogenomic case study we pursue in the article is a perfect exemplification of these obstacles. Compared to imaging and genomic measurements that are on the order of thousands and hundreds respectively, the number of intersecting samples for the two modalities of information is small ($n = 60$). First, estimates of uncertainty for the parameters within models post selection are no longer reliable unless inference accounts, precisely, for the preceding model-selection steps. This calls for “selection-aware inference” which overcomes the bias encountered during model-selection, documented in literature as one of the leading factors behind the replication crisis in science (Benjamini and Yekutieli, 2005; Berk et al., 2013; Lee et al., 2013). Second, reliable selection-aware inference involves an inevitable tradeoff of information within the data samples between the quality of model selection and inferential power. Clearly in all realistic scenarios, the extent to which this balance is accomplished has severe implications on the number of discoveries and the power of uncertainty estimates associated with the same findings. The inferential approach we take in this work achieves both these indispensable goals during integrative modeling and follow-up inference.

Selection-aware Bayesian framework and related works Anchored within a recently proposed conditional framework for Bayesian models (Yekutieli, 2012; Panigrahi et al., 2016), the inferential methods we adopt, reutilizes left-over information from selection towards uncertainty estimation. Post selecting a model, a posterior is at the core of the conceptual skeleton, formed by using a conditional likelihood in conjunction with a prior on the parameters within this model. We call this object a selection-aware posterior in our work. Specifically, the Bayesian approach we take here is distinctly different from frequentist inference post selection (Lee et al., 2013; Tian and Taylor, 2018; Lee and Taylor, 2014; Panigrahi et al., 2019), the latter line of work relying upon a pivot for interval estimation. Instead, we work with a strategically chosen conditional likelihood, and our technical workflow utilizes a reparameterization mapping to sample from a selection-aware posterior on a transformed space. Enabling compact analytic expressions for this posterior, the mapping used by our

methods facilitates tractable inference from our integrative models on very modest computing budgets.

Our Bayesian methods demonstrate the potential of reusing samples in an effective integrative modeling of outcomes and reducing the variance of the matched estimates in subsequent inference. This advance is a first of its kind in the domain of integrative Bayesian inference post selection to the best of our knowledge. The tradeoff between selection and inference our approach strikes here stands in stark contrast with sample splitting (Hurvich and Tsai, 1990, for example), a state-of-the-art strategy widely deployed by practitioners to counter the perilous effects of bias from model-selection. With sample sizes as small as 60, ignoring a fraction of the samples for either tasks no doubt is highly suboptimal for integrative inference. Our numerical experiments illustrate the advantages our methods enjoy over splitting at different resolutions in terms of the sharpness of models we recover and power of follow-up uncertainty estimation; see Figure 3 for a preview of their performance.

The remaining article is organized as follows. Section 2 outlines our modeling framework after we provide details on the selection algorithms leading to a flexible class of integrative models. Section 3 discusses a selection-aware posterior and develops the methodological core of our work by obtaining explicit analytic expressions for a working version of this posterior. Section 4 explores in depth the potential of our proposal by simulating integrative models that use the actual genomic and imaging measurements. Section 5 provides uncertainty estimates for parameters representing biologically critical gene pathways, which we recover post utilizing genomic associations with imaging phenotypes and clinical outcomes for LGG.

2 Modeling framework

To introduce notations, we let n denote the number of intersecting (patient) samples and let p and L represent the number of explanatory and intermediary phenotypic variables respectively. Recall, the explanatory and intermediary variables in our radiogenomic investigation are genomic variables and imaging phenotypes measured across the intersecting samples. Furthermore, we denote the outcome variable as $Y \in \mathbb{R}^n$, the matrix of explanatory variables for the n samples as $G \in \mathbb{R}^{n \times p}$ and the intermediate phenotype measurements for the

n samples as $I \in \mathbb{R}^{n \times L}$. Particularly, I_l represents the l -th column of I . Finally, let G_F be the matrix that includes the subset of columns of G present in $F \subset \{1, 2, \dots, p\}$.

Figure 1 presents a schematic representation of how the selection steps (Section 2.1) inform our integrative models (Section 2.2). First, we discuss an ℓ_1 -regularized variable se-

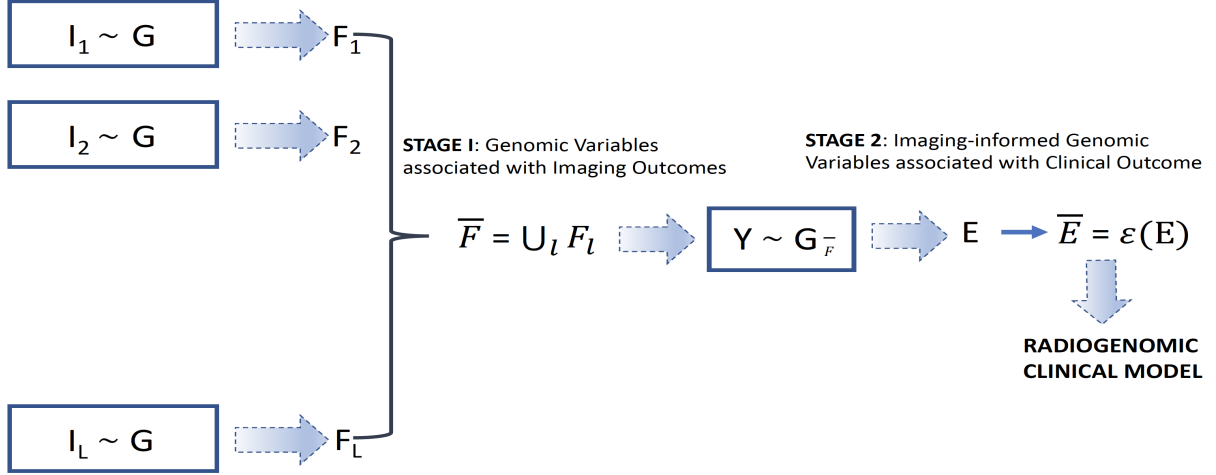


Figure 1: A schematic representation of the inputs and outputs of the selection pipeline divided into two stages. The first stage gives a candidate set of genomic variables associated with imaging phenotypes; the second stage selects promising variables from an imaging-informed set of genomic variables (from the first stage) that are statistically associated with the clinical outcome. The final output of the algorithm, E , imaging-informed genomic variables associated with the clinical outcome, (potentially) interacts with pre-existing knowledge about these p explanatory variables to determine our radiogenomic models.

lection pipeline to select an integrative model. The model we select automatically adapts to the sparsity of signals embedded in our high dimensional space of genomic covariates. Divided into two stages, the first step in this pipeline deploys a regression framework utilizing the intermediary phenotypic variables. This stage leads to a candidate set of promising explanatory variables, which we use for a sharp and meaningful downstream modeling of our response variable. In the second step, we select variables from this candidate set of explanatory variables that are informed by relevant associations with the intermediary phenotypes

and are further associated with the response. The output from this stage guides us to a flexible class of integrative models for inference.

2.1 Model-selection pipeline

Adopting a multiple regression framework based upon the intermediary phenotypic variables, we solve L LASSO queries (Tibshirani, 1996) as our start point. Note, I_l is the outcome variable in the l -th query. Let $\bar{F} = \cup_{l=1}^L F_l$, F_l denotes the promising explanatory variables selected on the basis of the following solution

$$(\hat{\alpha}_{F_l}, 0) = \arg \min_{\alpha} \|I_l - G\alpha\|_2^2 + \lambda_l \|\alpha\|_1 \text{ for } l = 1, 2, \dots, L; \quad (1)$$

λ_l is the tuning parameter for the ℓ_1 penalty. Thus, \bar{F} gives a candidate set of explanatory variables such that each variable is associated with at least one of the intermediary phenotypic variables.

We follow (1) with a randomized version of ℓ_1 -regularized regression (Tian and Taylor, 2018; Panigrahi et al., 2019, 2018; Tian et al., 2016) to introduce the key tradeoff between model-selection quality and inferential power with our available samples. Specially, such a strategy perturbs the canonical algorithm with a randomization variable $\mathcal{R} \sim N(0, \eta^2 \cdot I)$ independent of $(Y, I_l, 1 \leq l \leq L)$ as stated below:

$$(\hat{\beta}_E^{\text{LASSO}}, 0) = \arg \min_{\beta} \|Y - G_{\bar{F}}\beta\|_2^2 + \|\Lambda\beta\|_1 + \epsilon \cdot \|\beta\|^2/2 - \mathcal{R}^T \beta. \quad (2)$$

In this optimization, $\Lambda = \text{diag}(\lambda_1, \dots, \lambda_{|\bar{F}|})$ is a diagonal matrix with ℓ_1 -penalty weights for the $|\bar{F}|$ variables we select after harnessing associations with our intermediary phenotypes. Particularly setting these weights to be inversely proportional to the proportion of times an explanatory variable is selected across the L regularized queries in the previous step is one such concrete way to incorporate the relative importance of each variable in (2). Lastly, E represents the set of LASSO estimates not shrunk to zero, the explanatory variables informed by the associations with the intermediary variables and statistically associated with the outcome.

Noticeably, the optimization objective (2) differs from a canonical version of Lasso through an additional term, which is linear in the randomization instance \mathcal{R} and an ℓ_2

penalty with a small positive coefficient $\epsilon > 0$. We, in fact, use a small ℓ_2 penalty to ensure that the solution to the randomized problem does exist. This formulation easily accommodates a non-trivial version of the ridge penalty to impose an elastic net type-penalty. We showcase the effectiveness of randomized strategies in selecting sharp integrative models alongside construction of reliable and powerful uncertainty estimates later in our empirical analyses Section 4. Next we turn our attention to an integrative modeling framework based upon E , the final output of this two-stage pipeline.

2.2 Integrative Bayesian models post selection

We begin by noting that the pipeline in the previous discussion leads us to observe the following realizations for the selected sets of explanatory variables:

$$\widehat{E}(Y, \mathcal{R}; G_{\bar{F}}) = E \text{ where } \bar{F} = \cup_{l=1}^L \widehat{F}_l(I_l, G) \text{ and } \widehat{F}_l(I_l, G) = F_l, \quad (3)$$

clearly dependent on the data at our disposal. Define

$$\mathcal{E} : E \rightarrow \bar{E},$$

a mapping applied to E that returns \bar{E} , a subset of the p explanatory variables. This allows room to incorporate interactions between pre-existing knowledge about potentially important explanatory variables with the outputs from our variable selection pipeline in steps (1) and (2). For example, addition of variables using existing annotations about our genomic measurements, or previously deployed clinicals models to the selected set E will result in \bar{E} . In terms of modeling, the above mapping gives us added flexibility to leverage information about our explanatory variables, not observed otherwise from our data through the automated selections.

We assume a linear dependence model between Y and $G_{\bar{E}}$ such that each sample i is identically and independently distributed as

$$Y_i = G_{i, \bar{E}} \beta_{\bar{E}} + \epsilon_i, \text{ where } \epsilon_i \sim N(0, \sigma^2), \quad (4)$$

under a fixed predictor matrix framework. This is our primary outcome model of interest. Let $G_{i, \bar{E}}$ denote the i -th row of the matrix $G_{\bar{E}}$. For modeling the associations between the

intermediary and explanatory variables, we assume for now

$$I_{i,l} = G_{i;F_l} \alpha_{F_l} + \Psi_{i,l}, \quad 1 \leq l \leq L, \quad \text{where } (\Psi_{i,1}, \dots, \Psi_{i,L}) \stackrel{i.i.d.}{\sim} N(0, \Sigma_I), \quad (5)$$

and $\Psi_i = (\Psi_{i,1}, \dots, \Psi_{i,L})$ is independent of ϵ_i in the primary model of interest (4). Specifically, these intermediary phenotypic models inform our primary outcome model via F_l for $1 \leq l \leq L$, which in turn determine the explanatory variables during the automated selection procedure (2) for a downstream modeling of the response.

Completing the model specification in a Bayesian framework, we impose a rich family of Gaussian priors $\pi(\cdot)$ on our adaptive parameters $\beta_{\bar{E}}$:

$$\beta_{\bar{E}} \mid (\eta_1^2, \eta_2^2, \dots, \eta_{|\bar{E}|}^2)^T \sim N(0, \sigma^2 \text{diag}(\eta_1^2, \eta_2^2, \dots, \eta_{|\bar{E}|}^2)); \quad \eta_j^2 \sim N(0, \lambda^2), \quad j \in \bar{E}. \quad (6)$$

Marginalizing over $(\eta_1^2 \quad \eta_2^2 \quad \dots \quad \eta_{|\bar{E}|}^2)^T$ yields a prior for $\beta_{\bar{E}}$ (Park and Casella, 2008) that is proportional to

$$\prod_{j=1}^{|\bar{E}|} \exp(-(\sigma\lambda)^{-1} \cdot |\beta_{j;\bar{E}}|).$$

We note that this construction admits a flexible class of models based on the below aspects of our modeling assumptions.

Remark 1. *The variable mapping, \mathcal{E} is allowed to be a black box as long as it depends on the data only through output E from our regularized selection algorithms. Importantly, the interplay between pre-existing knowledge and the data-dependent outcome E need not be explicitly specified for selection-aware inference; all we need is the value of this mapping, \bar{E} under our modeling setup.*

Remark 2. *Second, the validity of our inferential approach is not tied to (5) – the selected linear model between the explanatory and intermediary variables. We remark that our methods rely only upon the independence between ϵ_i and Ψ_i for each data sample; the proof for Proposition 1 in the next Section underscores this observation. We specify a simplified form for our intermediary models only for the sake of simple exposition.*

3 Selection-aware posterior inference

We introduce a selection-aware posterior in this section. This allows us a principled reuse of samples from the model-selection stages through a likelihood aligned with the conditional

perspective to inference post selection (Lee et al., 2013; Tian and Taylor, 2018; Panigrahi and Taylor, 2019). We then provide analytic expressions for a working version of this posterior and the corresponding gradient, essential ingredients that a large family of Markov chain Monte Carlo sampling schemes warrant to compute estimates of uncertainty. Our main results in this section accomplish this goal by: 1) obtaining a tractable selection-aware posterior based upon a simplified conditional likelihood; see Theorem 1 and (7); 2) employing a reparameterization mapping to evaluate our selection-aware posterior for easily solvable and compact sampler-based updates; see Theorems 2 and 3.

3.1 Selection-aware posterior

Explicitly accounting for the selection-aware nature of our modeling framework, our Bayesian methods are based upon a posterior using a conditional likelihood (Panigrahi et al., 2016) as the centerpiece. Truncated to all data realizations that result in our primary model (4), the conditional likelihood in particular discards the information from our samples utilized during model selection (Lee et al., 2013). We state this likelihood in Proposition 1, a function of parameters $\beta_{\bar{E}}$ in the primary outcome model. In the value of this likelihood, $\mathbb{P}[\hat{E}(Y, \mathcal{R}; G_{\bar{F}}) = E | \beta_{\bar{E}}]$ particularly represents the probability of selecting the explanatory variables indexed by E after solving (2).

Proposition 1. *Define $\hat{\beta}_{\bar{E}} = (G_{\bar{E}}^T G_{\bar{E}})^{-1} G_{\bar{E}} Y$ to be the least squares estimate in the primary model (4) parameterized by \bar{E} . Let $\Sigma_{\bar{E}}$ be the covariance matrix of $\hat{\beta}_{\bar{E}}$. Then, under the modeling assumptions (4) and (5), a likelihood involving $\bar{\beta}_{\bar{E}}$ conditional upon observing the selected sets of variables*

$$\hat{F}_l(\mathcal{I}_l, G) = F_l \text{ for } 1 \leq l \leq L, \quad \hat{E}(Y, \mathcal{R}; G_{\bar{F}}) = E,$$

is proportional to

$$(2\pi)^{-|\bar{E}|/2} \cdot \det(\Sigma_{\bar{E}})^{-1/2} \cdot \exp(-(\hat{\beta}_{\bar{E}} - \beta_{\bar{E}})^T \Sigma_{\bar{E}}^{-1} (\hat{\beta}_{\bar{E}} - \beta_{\bar{E}})/2) \\ \times \left\{ \mathbb{P}[\hat{E}(Y, \mathcal{R}; G_{\bar{F}}) = E | \beta_{\bar{E}}] \right\}^{-1}.$$

Appending the prior in (6) to this likelihood results in our selection-aware posterior. We point out to our readers that any standard sampling scheme targeting this posterior involves

computing

$$\mathbb{P}[\widehat{E}(Y, \mathcal{R}; G_{\bar{F}}) = E \mid \beta_{\bar{E}}^{(d)}]$$

at the parameters $\beta_{\bar{E}}^{(d)}$ in each new draw (d) from the associated sampler. Inevitably entailing the probability of selection at every update, computationally efficient algorithms for uncertainty estimation necessitate our methodological developments.

3.2 A simplified conditional likelihood

First, we describe in Proposition 2 the intricate selection event that our likelihood (Proposition 1) is conditioned upon. With a slight abuse of notations, we denote as G_E the submatrix of $G_{\bar{F}}$ where the selected columns are indexed by E . Further, we let the coordinates that are not selected by the randomized LASSO (2) by $E^c = \bar{F} \setminus E$.

The selection of an active set E is associated with the event $\{(y, r) : \widehat{E}(y, r) = E\}$, described in terms of realizations of the response, y , and our randomization, r . Proposition 2 now characterizes this selection event as a union of polyhedral regions, determined by $\{U_{s_E}, V_{s_E}, W_{s_E}, t_{s_E} : s_E = \{-1, 1\}^{|E|}\}$. Detailed expressions for these matrices are included in the Supplementary material.

Proposition 2. *After solving (2), the selection event $\{(y, r) : \widehat{E}(y, r) = E\}$ under a fixed predictor matrix framework is equivalent to*

$$\bigcup_{s_E=\{-1,1\}^{|E|}} \left\{ U_{s_E} \widehat{\beta}_{\bar{E}} + V_{s_E} (r_E, r_{E^c})^T + W_{s_E} (\widehat{\beta}_{\bar{E}}^\perp, \widehat{\beta}_{E^c}^\perp)^T > t_{s_E} \right\},$$

where $\widehat{\beta}^\perp = G_{\bar{F}}^T y - G_{\bar{F}}^T G_{\bar{E}} \widehat{\beta}_{\bar{E}}$, $\widehat{\beta}_{\bar{E}} = (G_{\bar{E}}^T G_{\bar{E}})^{-1} G_{\bar{E}}^T y$.

Notably complicated in form, our problem of computing the probability of the selection event in our conditional likelihood is realizable harder with the constraints we identify in Proposition 2. As we show next, we are able to reduce these characterizing constraints to simple sign restrictions by recognizing some additional information that we can condition upon in our framework. Define

$$Q = \begin{bmatrix} G_E^T G_E + \epsilon I & G_E^T G_{E^c} \end{bmatrix}^T, p(b) = (Q^T Q)^{-1} Q^T \left(G_{\bar{F}}^T G_{\bar{E}} b + \widehat{\beta}^{\perp, \text{obs}} - (\Lambda_E s_E, \Lambda_{E^c} z^{\text{obs}})^T \right).$$

The probability of selection then takes the form of an integral over a domain restricted to sign constraints:

$$I(\beta_{\bar{E}}) = \int_{\text{sign}(w)=s_E} (2\pi)^{-|\bar{E}|/2} \cdot \det(\Sigma_{\bar{E}})^{-1/2} \cdot \exp(-(b - \beta_{\bar{E}})^T \Sigma_{\bar{E}}^{-1} (b - \beta_{\bar{E}})/2) \\ (2\pi)^{-|E|/2} \cdot \det(Q^T Q / \eta^2)^{1/2} \exp(-(w - p(b))^T Q^T Q (w - p(b)) / 2\eta^2) dw db.$$

We formalize the above claim in our next Theorem.

Theorem 1. *Consider the modeling assumptions specified by (4) and (5). Then, conditional upon*

$$\{\hat{E} = E, \text{sign}(\hat{\beta}_E^{\text{LASSO}}) = s_E, z = z^{\text{obs}}, \hat{\beta}^\perp = \hat{\beta}^{\perp, \text{obs}}\},$$

the likelihood of the least squares estimate $\hat{\beta}_{\bar{E}}$ is proportional to

$$\{I(\beta_{\bar{E}})\}^{-1} \cdot (2\pi)^{-|\bar{E}|/2} \cdot \det(\Sigma_{\bar{E}})^{-1/2} \exp\left(-(\hat{\beta}_{\bar{E}} - \beta_{\bar{E}})^T \Sigma_{\bar{E}}^{-1} (\hat{\beta}_{\bar{E}} - \beta_{\bar{E}})/2\right).$$

The simplified probability of selection, $I(\beta_{\bar{E}})$ nonetheless still lacks a readily available closed form. To obtain a working version of the likelihood in Theorem 1, we borrow the recently proposed approximation to this object (Panigrahi and Taylor, 2019, see Proposition 3.1) with theoretical guarantees of concentrating around the generative parameters as sample size grows to infinity. Deferring further details of this approximation to the Supplementary material B, using this working expression for our (log-) likelihood in conjunction with our prior finally gives rise to a tractable version for the selection-aware posterior. Ignoring an additive constant, the logarithm of our posterior is given by

$$\log \pi(\beta_{\bar{E}}) - (\hat{\beta}_{\bar{E}} - \beta_{\bar{E}})^T \Sigma_{\bar{E}}^{-1} (\hat{\beta}_{\bar{E}} - \beta_{\bar{E}})/2 \\ + \inf_{b,w} \left\{ (b - \beta_{\bar{E}})^T \Sigma_{\bar{E}}^{-1} (b - \beta_{\bar{E}})/2 + (w - p(b))^T Q^T Q (w - p(b)) / 2\eta^2 + C_{s_E}(w) \right\}. \quad (7)$$

3.3 Posterior formulation via a transformation of parameters

Our next goal is to obtain compact analytic expressions for our working version of the selection-aware posterior in (7) and the corresponding gradient via a non-trivial reparameterization mapping. Precisely, this gives us samples on a transformed space when standard sampling techniques are applied for uncertainty estimation. The core computing step involves an $|E|$ -dimensional optimization problem, thus reducing the effective dimension of

inferential updates to the selected size of explanatory variables from our mining pipeline. This is undoubtedly orders smaller than the high dimensional start set of p potential variables. With no additional cost, we can easily reconstruct using the same map our original targets, the parameters in our adaptive model.

From now on, we denote

$$p(b) = Pb + o;$$

$$P = (Q^T Q)^{-1} Q^T G_{\bar{F}}^T G_{\bar{E}}, \quad \text{and } o = (Q^T Q)^{-1} Q^T \left(\hat{\beta}^{\perp, \text{obs}} - (\Lambda_E s_E, \Lambda_{E^c} z^{\text{obs}})^T \right).$$

Define a reparameterization map

$$\zeta_{\bar{E}} = \Psi^{-1}(\beta_{\bar{E}})$$

where $\Psi : \zeta_{\bar{E}} \rightarrow \beta_{\bar{E}}$ is given by

$$\beta_{\bar{E}} = \Psi(\zeta_{\bar{E}}) = (I + \eta^{-2} \Sigma_{\bar{E}} P^T Q^T Q P) \zeta_{\bar{E}} + \eta^{-2} \Sigma_{\bar{E}} P^T Q^T Q (o - w^*(\zeta_{\bar{E}})) \quad (8)$$

and

$$w^*(\zeta_{\bar{E}}) = \underset{w}{\operatorname{argmin}} \ (w - p(\zeta_{\bar{E}}))^T Q^T Q (w - p(\zeta_{\bar{E}})) / 2\eta^2 + C_{s_E}(w).$$

To bring out the distinction with (7), we denote the corresponding transformed (log-) posterior in Theorem 2 by $\log \tilde{\pi}(\zeta_{\bar{E}} | \hat{\beta}_{\bar{E}})$.

Theorem 2. Define a change of variables from $\beta_{\bar{E}} \rightarrow \zeta_{\bar{E}}$ via the reparameterization in (8).

Let $\mathcal{J}(\zeta_{\bar{E}})$ be given by

$$(I + \eta^{-2} \Sigma_{\bar{E}} P^T Q^T Q P) - \eta^{-4} \Sigma_{\bar{E}} P^T Q^T Q (\eta^{-2} Q^T Q + \nabla^2 C_{s_E}(w^*(\zeta_{\bar{E}})))^{-1} Q^T Q P. \quad (9)$$

Then, the logarithm of our working selection-aware posterior (7) as a function of the transformed parameters $\zeta_{\bar{E}}$ (up to a constant) equals

$$\begin{aligned} & \log \pi(\Psi(\zeta_{\bar{E}})) + \log |\det(\mathcal{J}(\zeta_{\bar{E}}))| + \hat{\beta}_{\bar{E}}^T \Sigma_{\bar{E}}^{-1} \Psi(\zeta_{\bar{E}}) - \zeta_{\bar{E}}^T \Sigma_{\bar{E}}^{-1} \Psi(\zeta_{\bar{E}}) \\ & + \zeta_{\bar{E}}^T \Sigma_{\bar{E}}^{-1} \zeta_{\bar{E}} / 2 + (w^*(\zeta_{\bar{E}}) - P \zeta_{\bar{E}} - o)^T Q^T Q (w^*(\zeta_{\bar{E}}) - P \zeta_{\bar{E}} - o) / 2\eta^2 + C_{s_E}(w^*(\zeta_{\bar{E}})). \end{aligned}$$

Our next Theorem obtains a compact expression for the gradient of this working version of the selection-aware posterior in terms of the transformed parameters $\zeta_{\bar{E}}$. Before we state this result, let $\tilde{C}_{s_E}(w^*(\zeta_{\bar{E}}))$ be a diagonal matrix such that the l -th diagonal entry equals $\nabla^3 B_l(w^*(\zeta_{\bar{E}}))$; let $\text{diag}(V)$ be a diagonal matrix with the vector V along the diagonal. Denote $N = \eta^{-2} Q^T Q + \nabla^2 C_{s_E}(w^*(\zeta_{\bar{E}}))$ and let the j -th column of $\eta^{-2} N^{-1} Q^T Q P$ be \mathcal{J}_j .

Theorem 3. Let $\mathcal{J}(\zeta_{\bar{E}})$ be given by (9) in Theorem 2 and let $\mathcal{M}_j(\zeta_{\bar{E}})$ equal

$$\text{Trace}\left(\eta^{-4}\mathcal{J}^{-1}(\zeta_{\bar{E}})\Sigma_{\bar{E}}P^TQ^TQN^{-1}\left(\tilde{C}_{s_E}(w^*(\zeta_{\bar{E}}))\cdot\text{diag}(\mathcal{J}_j)\right)N^{-1}Q^TP\right)$$

for $j = 1, 2, \dots, |\bar{E}|$. Under the reparameterization map $\beta_{\bar{E}} \rightarrow \zeta_{\bar{E}}$ in (8), the gradient of our (log-) selection-aware posterior in Theorem 2 is given by

$$(\mathcal{J}(\zeta_{\bar{E}}))^T \left(\nabla \log \pi(\Psi(\zeta_{\bar{E}})) + \Sigma_{\bar{E}}^{-1} \hat{\beta}_{\bar{E}} - \Sigma_{\bar{E}}^{-1} \zeta_{\bar{E}} \right) + \left(\mathcal{M}_1(\zeta_{\bar{E}}) \ \dots \ \mathcal{M}_{|\bar{E}|}(\zeta_{\bar{E}}) \right)^T.$$

With a sample $\zeta_{\bar{E}}^{(d)}$ from our working selection-aware posterior in Theorem 2, we obtain the corresponding draw for our target parameter $\beta_{\bar{E}}^{(d)}$ using (8). We observe that a reconstruction of our original target parameters does not lead to an additional cost, since it simply relies upon the optimizer $w^*(\zeta_{\bar{E}}^{(d)})$ which we calculate in the expression of our transformed posterior. We therefore indicate that solving for $w^*(\cdot)$ contributes to the major computing cost towards selection-aware inference. Viewing this from the perspective of sampling efficiency, the optimization at every update of the transformed posterior is indeed only $|\bar{E}|$ -dimensional, the size of the promising explanatory variables we work with at the end of our selection pipeline.

4 Simulation analysis

We turn our attention in this section to a reconciliation between the selection-aware nature of our Bayesian models and the validity of inferential estimates that our methods facilitate in empirical analyses. We discuss our design of experiment, demonstrate the potential of the proposed machinery in terms of in-depth inferential comparisons with naive uncertainty estimates and sample-splitting at a range of resolutions, and illustrate how these inferential metrics successfully generalize to dimensions distinct from the radiogenomic application under scrutiny.

4.1 Simulation design

Generating a sparse model with both weak and strong signals of varying amplitudes and random signs, we draw in each round of simulation an outcome from the primary model (4).

The signal vector β is generated from a mixture of centered Laplace distributions, the true underlying prior. That is, each coordinate is drawn as follows

$$\beta_j \sim \Pi_j(\cdot) := \pi \cdot \text{Laplace}(0, 0.10) + (1 - \pi) \cdot \text{Laplace}(0, s) \text{ for } 1 \leq j \leq r; \quad (10)$$

$r = |\bar{F}|$. Changing the scale of one of these Laplace distributions, s and the mixing proportion, π results in different signal regimes. The sparsity levels of our signal vector is controlled by the mixing proportion.

We vary in our simulation design the ratio between the number of our samples, n and the number of regressors, r before screening out the set E to determine the primary model (4) in conjunction with domain knowledge. We investigate specifically the sample sizes $n = 180, 360, 720$ to match the dimension ratio $r/n = 2, 1, 0.5$ respectively. For the real data analysis, note that $r/n \approx 5$, $n = 60$, $r = 357$. In this case, the predictor matrix we use is indeed based on the real values of genomic and radiomic measurements. Details on the acquisition of this data are included in the next section. To generate predictor measurements for sample sizes larger than 60, we append synthetic design values to the real design matrix in order to achieve the studied regression dimensions. Specifically, we draw $x_i \in \mathbb{R}^r, 1 \leq i \leq n_1$ such that $x_i \sim N(0, \Sigma(\rho))$, for $i = 1, 2, \dots, n_1$ and n_1 is chosen so that $r/(n_1 + n) = 2, 1, 0.5$ in the three case studies of interest; $\Sigma(\rho)$ is an autocorrelation covariance matrix such that the $\Sigma_{i,j} = \rho^{|i-j|}$ and $\rho = 0.70$.

Our strategy to reflect a realistic data generation process through simulations is aligned along the following principles. First, we note that the variability in the outcome variable is explained by multiple markers, consistent with our expectation of a polygenic response variable. Second, the generative model we use incorporates a mix of weak and strong signals with varying amplitudes and random signs. This enables us to investigate the genuine ability of our inferential method to adapt to the strength of the signals present in the data and to reconstruct efficiently the corresponding effect sizes. Finally, admitting different regression dimensions, our simulations showcase (i) the necessity of adopting our methods even in moderate dimensions where a severe impact of selection bias is seen and (ii) our methods support a greater number discoveries, with clearly shorter and hence more powerful inferential estimates than the benchmark approach of splitting deployed widely by practitioners.

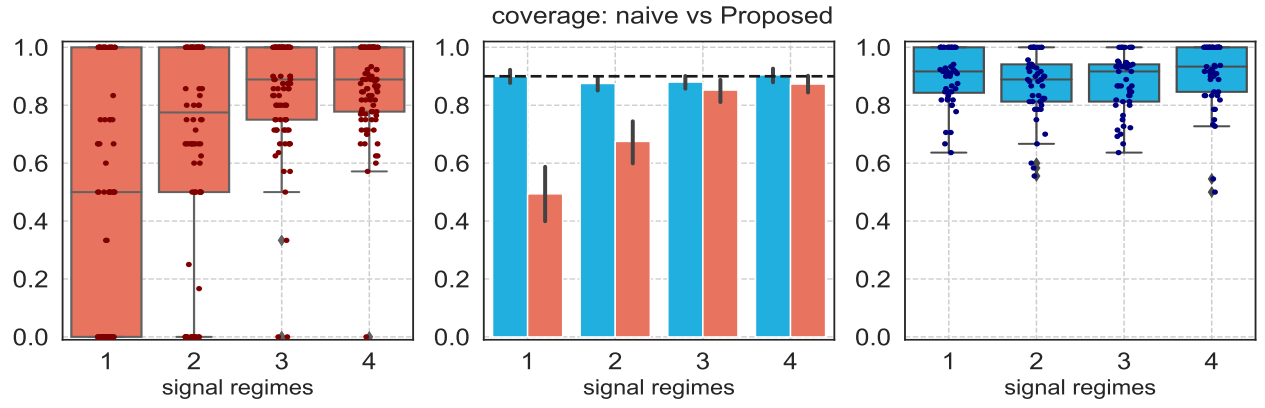
4.2 Empirical analysis: consistent with radiogenomic case study

We begin by exploring our methods with the real radiogenomic predictors, simulating $n = 60$ samples to agree closely with our radiogenomic application. Selecting an integrative model using the mining pipeline in Section 2.1 and employing the proposed Bayesian machinery with a selection-aware posterior at the core, we bring to the fore the advantages of adopting a selection-aware approach using all the data. Noteworthy in our results is the balance in the sharpness (quality) of model and associated inferential power, imminent when a finite amount of data must be allocated for deciding upon a model as well as conducting inference.

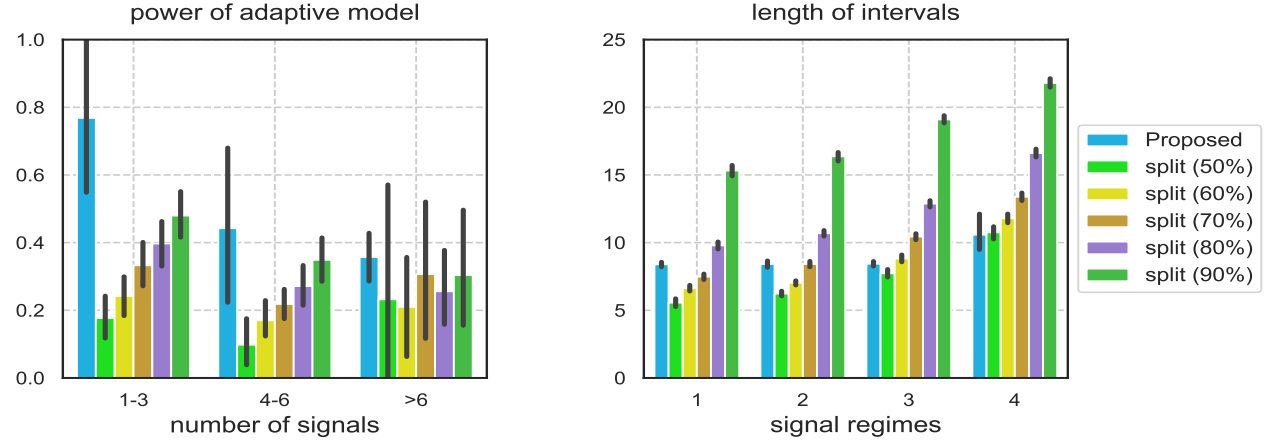
We set the randomization variation η^2 in (2) to be equal to the noise level in the outcome (estimated from data). Below, we present detailed comparisons of our approach with sample-splitting. Setting $\pi = 0.95$ in the true generative scheme (10) and varying the variance of the Laplace distribution between $\{0.20, 1, 2, 4\}$, we consider 4 signal regimes—numbered 1-4 on the x-axis of Figure 2. Utilizing the expressions of the reparameterized version in Theorems 2 and 3, we construct intervals for $\beta_{\bar{E}}$ in the model specified by (4) and (6), where $\bar{E} = E$ is the final output of the regularized variable selection algorithms.

Figure 2 anchors the motivation behind using a selection-aware posterior in panel (I). The distribution of the empirical coverages of naive interval estimates that do not account for the selection-aware nature of integrative models have averaged coverage falling way short of the benchmark target of 90%. The interval estimates furnished by our methods support the validity and necessity of the inferential proposal in the article. Panel (II) exemplifies a significantly better reconciliation between the sharpness of the model recovered from integrative analysis and subsequent inferential power in comparisons with splitting when different proportions of data are utilized for selection and inference. Specifically, the performance of the rather unconventional randomized query (2) in terms of model selection is evaluated using the number of true signals screened under different sparse scenarios. The follow up inferential power is measured as the averaged lengths of interval estimates.

Observe, splitting where 90% of the data is assigned for selecting signals is the best performer amongst all the split-based methods in terms of model-selection. However, this power is clearly dominated by the randomized scheme we adopt for modeling. In an assessment of



(I)



(II)

Figure 2: (I): Invalidity of naive inference (in orange)– the x-axis represents different signal regimes and the y-axis plots empirical coverage of 90%-intervals across the regimes. Left panel shows the distribution of naive estimates that ignore adaptive nature of model; central panel compares the averaged coverages across the regimes; right panel plots empirical distribution of the proposed intervals. The dotted line at 0.90 is the nominal coverage. (II): Tradeoff in model selection and inferential power– left panel highlights the quality of our integrative model measured via the screening power of true signals; right panel shows the distribution of averaged lengths of interval estimates in the selected model.

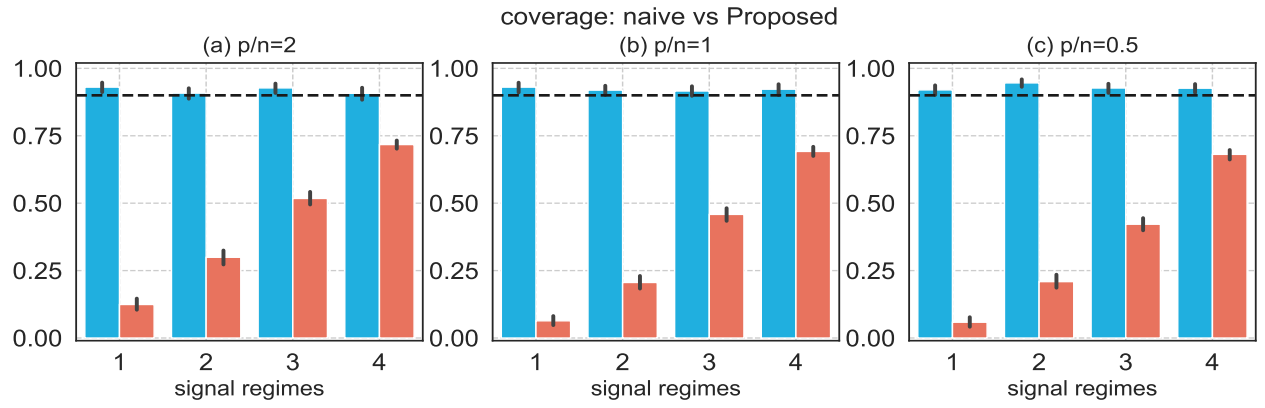
inferential power, our methods correcting appropriately for the selection bias provide interval estimates that are less than half the length of the 90% split-based intervals. An important take away is the attractive alternative that our methods offer in comparison to splitting at sample proportions across the range of resolutions in terms of data allocation for the two core tasks. Quite evidently we allow a distinctly unique yet more efficient tradeoff in the use of information for modeling and follow-up uncertainty estimation.

4.3 Inferential results: an illustration of our scope

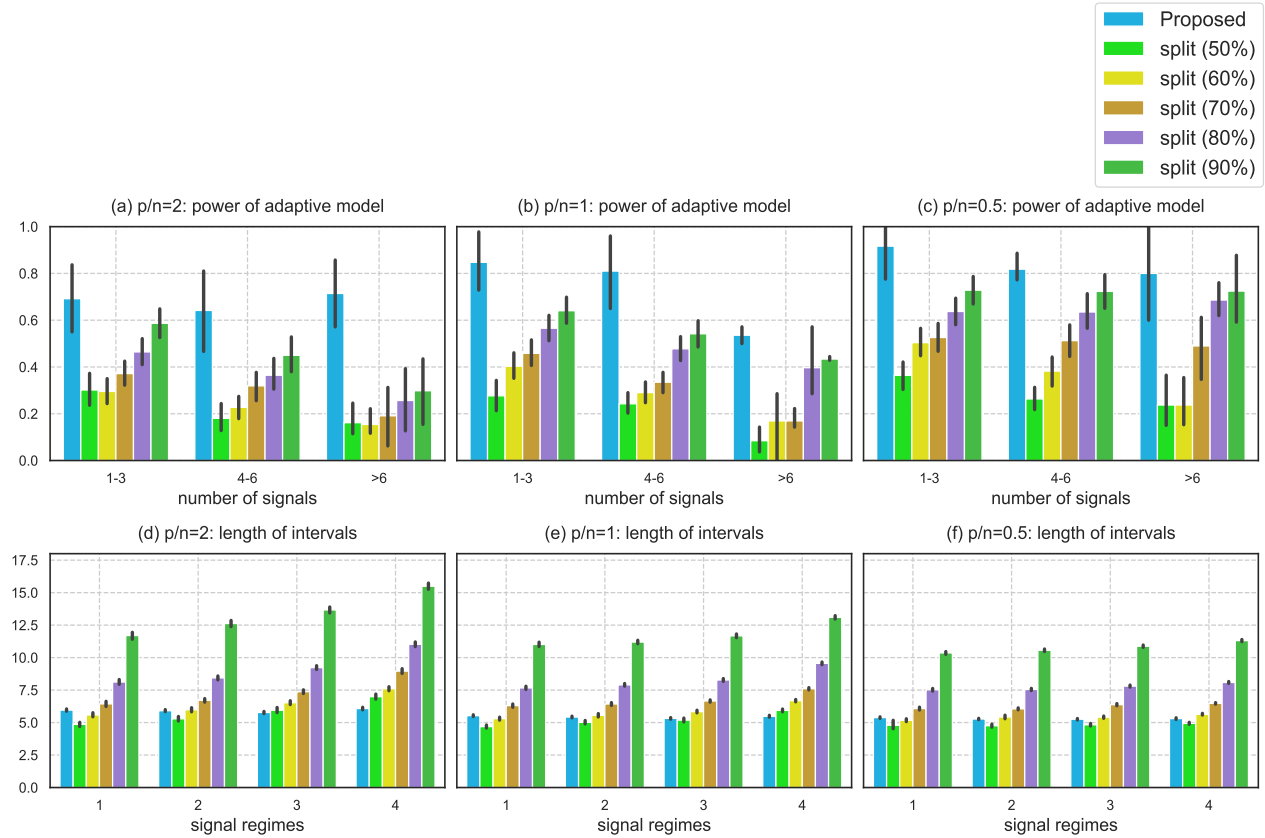
We next demonstrate how our methods generalize in their application to other data dimensions beyond our focused study. Figure 3 emphasizes the strong need to correct for selection bias when we compute the averaged coverages of naive and Proposed intervals across the regression dimensions $r/n = 2, 1, 0.5$. For the signal regimes described in our simulation design, we see a severe shortfall of coverage for the naive interval estimates, ranging as low as $\sim 10\%$ and increasing to a level of only $\sim 70\%$ in the moderate SNR regimes. We remark here that the coverage of the naive intervals worsens in comparison to the case study analyzed under Section 2. This difference in the behavior of the naive intervals can be attributed to the synthetic predictor values we append to the real radiogenomic observations in the simulations in order to vary the size of regression.

In panel (II) of the same Figure, we highlight 1) the sharpness of the selection-aware model in (a), (b), (c) in terms of the number of signals screened by the randomized strategy (2) and split-based schemes and 2) inferential power in (d), (e), (f) measured as the averaged lengths of the interval estimates produced by the Bayesian machinery in the paper when compared to state-of-art splitting. Coherent with the findings in the preceding discussion, the proposed methods dominate all the split-based methods when assessed for the quality of the selected model; the percentage in the legend indicates the proportion of samples used for model selection.

In balancing the allocation of samples towards the two tasks of model selection and inference, splitting based on 90% of the samples for selection produces the best model amongst the split-based strategies. Yet, this split-based method falls short of the randomized selection in terms of the quality of the primary model of interest. Comparing the averaged lengths



(I)



(II)

Figure 3: (I): The x-axis represents different signal regimes and the y-axis plots empirical coverage of 90%-intervals; dotted line at 0.90 is the target coverage. (II): Evaluation of selected model in Panels (a), (b), (c) and inferential power in Panels (d), (e), (f).

of the interval estimates in the four signal regimes and under the different regression dimensions, we note that the selection-aware Bayesian inferential methods yield intervals that are shorter by two-three times than split (90%). On the other hand, choosing a split-based approach with 50% of the samples devoted for model selection results in a relatively worse model for inference, leading to lesser discoveries left out in the selection stage. Figure 3 yet again summarizes the advantages our selection-aware techniques enjoy over the common practice of splitting the data into two parts. The conditioning after randomizing corrects precisely for the selection of a sharp model with relevant parameters and permits an optimal reuse of data samples during inference at the same time.

5 Radiogenomic analysis for LGG

We conduct our radiogenomic empirical analysis with the real samples and the genomic features and radiomic phenotypes capture complementary characteristics of the underlying tumor. These measurements are collectively harnessed in integrative models to assess associations with relevant clinical endpoints such as disease progression, survival time etc. for the patients. We provide the details related to data acquisition and pre-processing of both the imaging and genomic modalities with specifics largely deferred to Supplementary material C. We follow this up with an implementation of our inferential machinery in Section 5.2 post an integrative mining pipeline. Lastly, we give biological insights into our radiogenomic findings and place the relevance of the resulting effect size estimates in the context of recent scientific literature in Section 5.3.

5.1 Pathway scores and radiomic phenotypes

We obtain the genomic data from LinkedOmics (Vasaikar et al., 2017), a publicly available portal that includes multi-omics data from multiple cancer types in TCGA. The genomic data we acquire are normalized gene-level RNA sequencing data from the Illumina HiSeq system (high-throughput sequencing) with expression values in the \log_2 scale. Focusing on subjects with LGG, the gene expression data includes 516 samples and 20086 genes, which is narrowed down further to the intersecting samples with imaging phenotypes in an integrative

study.

A set of genes broadly constitutes a gene pathway. In our case, we derive the pathway membership of genes from the Molecular Signature Database (Liberzon et al., 2011), a publicly available resource containing annotated gene-sets divided into multiple collections (groups of pathways). Particularly, we consider four collections namely Hallmark Pathways (50 pathways), KEGG Canonical Pathways (KEGG - 186 pathways), Cancer Gene Neighborhoods and Cancer Modules (C4 - 858 pathways), and Oncogenic Signatures (C6 - 189 pathways). In Supplementary material C.1, we discuss the construction of pathway scores for these genomic measurements.

For the imaging records, we obtain the pre-operative multi-institutional MRI scans of TCGA LGG collection available in TCIA (Clark et al., 2013). For our analysis, we consider four types of MRI sequences which include (i) native (T1), (ii) post-contrast T1-weighted (T1Gd), (iii) T2-weighted (T2), and (iv) T2 fluid attenuated inversion recovery (FLAIR) volumes. Each of these sequences display different types of tissues with varying contrasts based on the tissue characteristics. From the whole brain MRI scans, the tumor regions can be identified using an automated segmentation method called GLISTRboost (Bakas et al., 2015, 2017). These segmentation labels additionally identify each voxel as one of the three tumor sub-regions namely, necrotic and non-enhancing tumor core (NC), the peritumoral edema (ED) and the enhancing tumor (ET). In Figure 6, we show an axial slice from the MRI scan of a LGG subject corresponding to all four imaging sequences as well as the segmented tumor sub-regions.

The voxel intensity values so obtained are sensitive to the configuration of the MRI machine and are difficult to interpret. These values are neither comparable across different subjects, nor between study visits for the same subject. We address this issue by implementing a biologically motivated normalization technique called white-stripe normalization (Shinohara et al., 2014). Finally, we work with the intensity values corresponding to each of the 12 group of voxels (4 MRI sequences and 3 tumor sub-regions) separately. For each of the 12 groups of intensity values, we construct kernel density estimates for all the 61 subjects. These densities give rise to the principal component scores for each of the 12 groups separately, whose details are included in Supplementary material D.1.

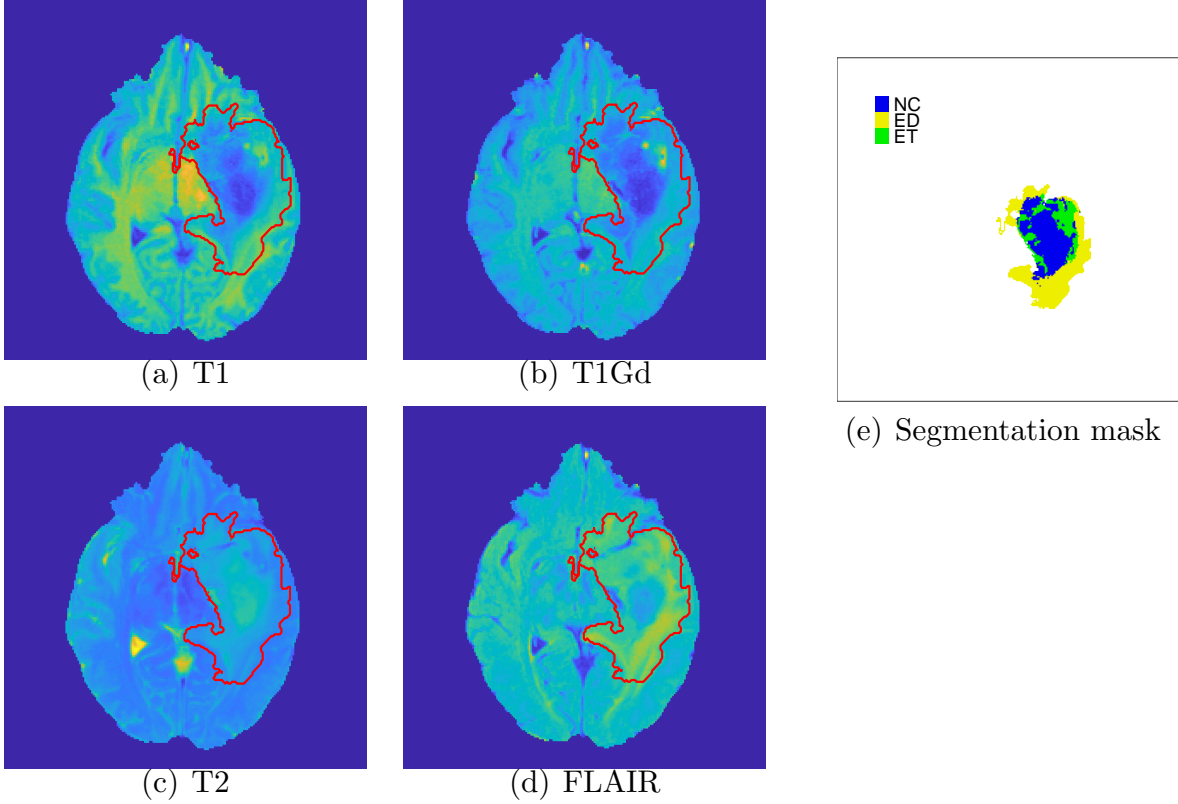


Figure 4: An axial slice of a brain MRI from four modalities: T1, T1Gd, T2 and FLAIR for a LGG subject. The segmented tumor region is shown with an (red) overlaid boundary. Segmentation mask indicates the necrotic and non-enhancing tumor core (NC), the peritumoral edema (ED) and the enhancing tumor (ET) regions.

5.2 Selection-aware pipeline with radiogenomic characteristics

The first stage of the integrative mining pipeline begins by identifying a set of promising pathways associated with the radiomic-based intermediary phenotypes. Our start point is solving (1) with the 143 principal component scores across the 12 groups of tumor voxels as responses, regressed against 1289 pathways from the four pathway collections (Hallmark, KEGG, C4, and C6). The output of this step is a set of 369 gene pathways, each of which is associated with one or more of the radiomic phenotypes. These are promising candidates setting up the second stage of our mining pipeline where associations with the outcome of interest are evaluated. Of these 369 pathways selected, the multiplicity of each pathway defined as the number of LASSO queries which selects this potential predictor, ranging

$\sim 1 - 9$.

The second stage (2) deploys a randomized version of LASSO to partition the information within the data towards selecting a model, followed by reliably calibrating strengths of these selected associations. The penalty weights in the LASSO are set to be inversely proportional to the multiplicity of a pathway, in order to reflect an importance weight for that feature in terms of its association with the imaging scores. We select 15 pathways from this second stage regression, the imaging informed set of explanatory variables representative of the variability in the clinical response. Setting $\bar{E} = E$ in (4) and using the prior in (6), and ultimately, relying upon the analytic formula for the corrected posterior in (2), we obtain samples from the posterior adjusted precisely for selection bias. Inference for the adaptively determined parameters β_E now enables effect size estimates corresponding to the 15 reported pathways. In Figure 5 we showcase the bounds for 50%, 80% and 95% credible intervals based on the MCMC samples for the 15 reported pathways.

5.3 Biological Interpretations

We now focus on some of our findings, providing their biological implications and interpreting the same in the context of existing clinical knowledge in this domain.

1. We see that the gene pathway, Vascular Smooth Muscle Contraction, from the KEGG collection has significant association with overall survival. Vascular smooth muscle cell (VSMC) is a highly specialized cell whose principal function is contraction. These cells shorten on contraction, consequently decreasing the diameter of a blood vessel to regulate the blood flow and pressure. Moreover, in a clinically relevant mouse model of glioma, it was found that the glioma cells disrupt the VSMCs as they populate the perivascular space of preexisting vessels, causing a focal breach in the blood brain barrier (Watkins et al., 2014). It has been demonstrated that endothelial specific growth factor such as, vascular endothelial growth factor (VEGF), can interact with non-endothelial cells and play a role in modulating the response of VSMCs (Ishida et al., 2001). VEGF expression levels were associated with the presence of ringlike tumor contrast enhancement, which present phenotypically as variable contrast on T1Gd MRI scan and were jointly associated

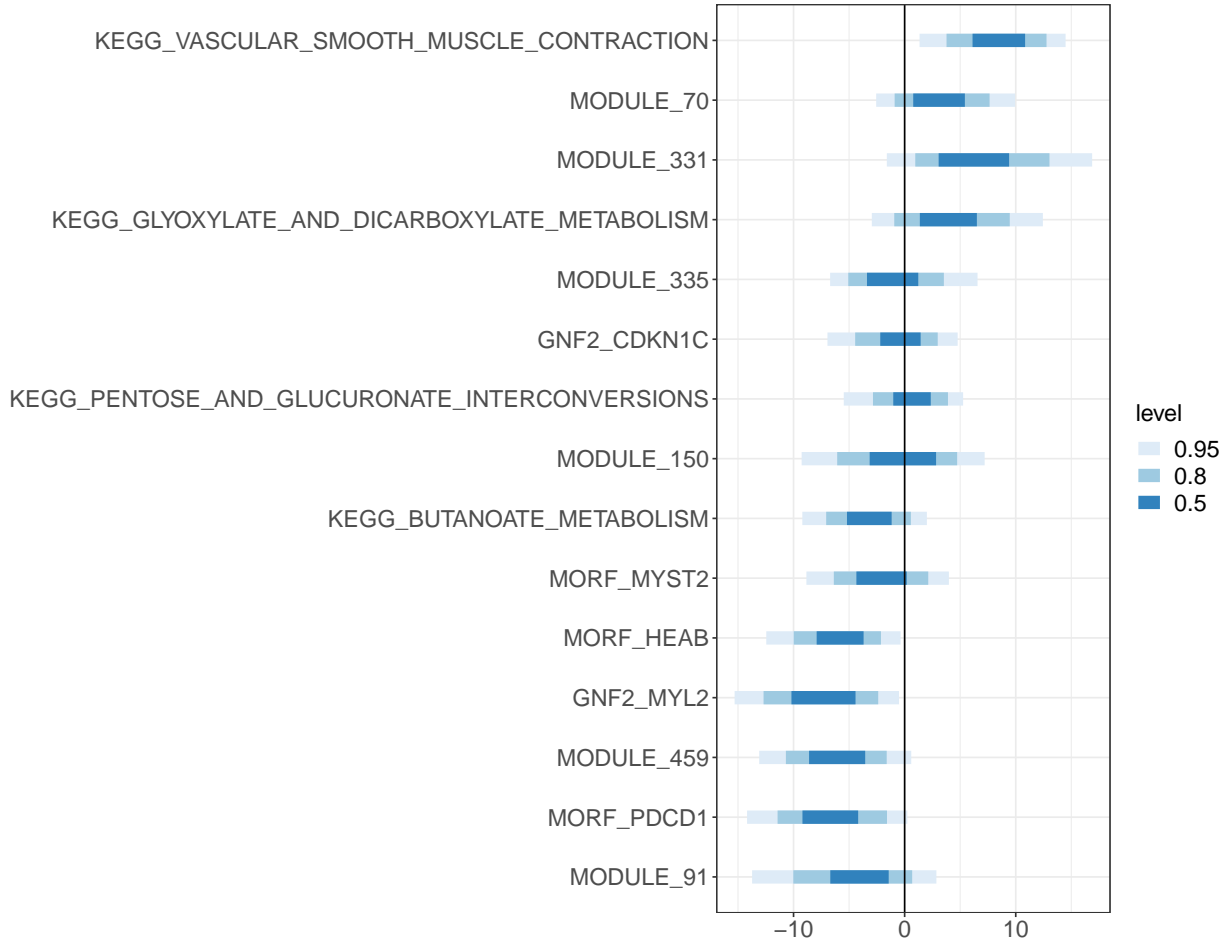


Figure 5: Bounds of the credible intervals for the gene pathways associated with the overall survival and with the radiomic characteristics.

with progression-free survival in glioblastoma (Wang et al., 2016).

2. The gene pathway denoted as MORF PDCD1 which includes the genes in the neighborhood of the gene PDCD1, is seen to have a significant association with the overall survival. Recent work (Röver et al., 2018) indicates that PDCD1 promoter methylation is a prognostic factor in LGG with Isocitrate Dehydrogenase (IDH) mutations. It is known that high expression of PDCD1 on the immune cells infiltrating the LGG is a marker for immune evasion and associated with survival.
3. Another significant association we notice in our analysis corresponds to the gene pathway GNF2 MYL2. This is a group of genes in the neighborhood of MYL2 (myosin light chain

II). Previous studies Beadle et al. (2008) show that myosin II plays a significant role in glioma invasion in vivo, where it regulates the deformation of the nucleus as well as the membrane of glioma cells. This has been further validated through mathematical modeling in recent literature (Lee et al., 2017). Notably the extent of immune/inflammatory activity is reflected through the edema region on MRI scan (Kleijn et al., 2011).

Some of the other pathways associated with the overall survival include metabolic pathways from KEGG such as (a) pentose and glucuronate interconversions, (b) glyoxylate and dicarboxylate metabolism, and (c) butanoate metabolism. In light of the significant role that metabolic reprogramming plays in glioma pathogenesis (Strickland and Stoll, 2017), it is encouraging to see that a number of metabolic pathways are identified to be significantly associated with patient prognosis. From the pathways for cancer gene neighborhoods we see significant associations with the gene pathways such as neighborhoods of (a) MYST2, a histone acetyltransferase that plays crucial functions in transcription, DNA replication and repair, and (b) CDKN1C, which is known to regulate several of the hallmark properties of cancer (Kavanagh and Joseph, 2011). A follow-up validation of these pathways will illuminate nuances in understanding the tumor etiology under study.

6 Concluding remarks

In this work, we propose a post-selective approach to integrative Bayesian modeling of high dimensional data. Integrative investigations across different modes of information have the potential to identify biological underpinnings and reveal their relationships with patient outcomes in several disease domains. In the specific context of cancer, associations between genomics and radiomics collectively throw light on how these inter-related features correlate with clinically relevant endpoints and inform models with better prognostic abilities. Nevertheless integrative analyses face several barriers from an inferential perspective, including sharp modeling in low SNR regimes, enabling coherent inference post selection of such models and efficient use of information for both model-selection and subsequent inference.

We address the above challenges through a selection-aware posterior, defined after a regularized model search leveraging intermediary phenotypes. Yet our posterior is crafted

prudently, to account precisely for the selection-aware nature of the integrative model. Faced with the lack of compact analytic expressions for the corrected form of the posterior, we provide formulae that a very general class of samplers can employ for statistically accurate uncertainty estimation. The results applied to model links between gene pathways and patient outcomes using associations with the radiomic phenotypes are quite promising in both statistical and computational terms. Integrative models with a focused set of relevant parameters no doubt lead to more scalable and easy to interpret findings. In reusing these samples, we showcase a unique and effective partitioning of our available data for modeling and follow-up inference through a conditional perspective after selection. Detailed comparisons with splitting at different resolutions particularly highlight how our proposal fares in this inevitable tradeoff in data. The accompanying code and data for our methods will be disseminated for reproducibility of our selection-aware pipeline.

We conclude by remarking that there is certainly room for future directions. The tractability of our selection-aware methods will accommodate complicated joint models involving both radiomic and genomic features. Relating the clinical outcomes to the various radiogenomic markers in such models will possibly throw new light on how these features interact together to impact the underlying response. Further, a framework to borrow structure shared between the different radiomic measurements will prompt use of other structure inducing penalties distinct from an ℓ_1 -type regularization. We leave these problems for interesting future explorations.

7 Acknowledgements

S.P. acknowledges support through NSF-DMS 1951980. S.M., A.R and V.B. were supported through CCSG P30 CA046592, Precision Health Scholar award (to S.M), Institutional Research Grants from The University of Michigan, NCI R37CA214955-01A1, and a Research Scholar Grant from the American Cancer Society (RSG-16-005-01). V. B. was also supported by NIH grants R01-CA160736, R21-CA220299, NSF grant 1463233, and start-up funds from the U-M Rogel Cancer Center and School of Public Health.

References

Baek, H. J., Kim, H. S., Kim, N., Choi, Y. J., and Kim, Y. J. (2012). Percent change of perfusion skewness and kurtosis: a potential imaging biomarker for early treatment response in patients with newly diagnosed glioblastomas. *Radiology* **264**, 834–843.

Bakas, S., Akbari, H., Sotiras, A., Bilello, M., Rozycki, M., Kirby, J. S., Freymann, J. B., Farahani, K., and Davatzikos, C. (2017). Advancing the cancer genome atlas glioma mri collections with expert segmentation labels and radiomic features. *Scientific data* **4**, 170117.

Bakas, S., Zeng, K., Sotiras, A., Rathore, S., Akbari, H., Gaonkar, B., Rozycki, M., Pati, S., and Davatzikos, C. (2015). Glistrboost: combining multimodal mri segmentation, registration, and biophysical tumor growth modeling with gradient boosting machines for glioma segmentation. In *BrainLes 2015*, pages 144–155. Springer.

Beadle, C., Assanah, M. C., Monzo, P., Vallee, R., Rosenfeld, S. S., and Canoll, P. (2008). The role of myosin ii in glioma invasion of the brain. *Molecular biology of the cell* **19**, 3357–3368.

Benjamini, Y. and Yekutieli, D. (2005). False discovery rate–adjusted multiple confidence intervals for selected parameters. *Journal of the American Statistical Association* **100**, 71–81.

Berk, R., Brown, L., Buja, A., Zhang, K., Zhao, L., et al. (2013). Valid post-selection inference. *The Annals of Statistics* **41**, 802–837.

Bhattacharyya, A. (1943). On a measure of divergence between two statistical populations defined by their probability distributions. *Bull. Calcutta Math. Soc.* **35**, 99–109.

Clark, K., Vendt, B., Smith, K., Freymann, J., Kirby, J., Koppel, P., Moore, S., Phillips, S., Maffitt, D., Pringle, M., et al. (2013). The cancer imaging archive (tcia): maintaining and operating a public information repository. *Journal of digital imaging* **26**, 1045–1057.

Dryden, I. and Mardia, K. (1998). *Statistical analysis of shape*. Wiley.

Gentleman, R. C., Carey, V. J., Bates, D. M., Bolstad, B., Dettling, M., Dudoit, S., Ellis, B., Gautier, L., Ge, Y., Gentry, J., et al. (2004). Bioconductor: open software development for computational biology and bioinformatics. *Genome biology* **5**, R80.

Gevaert, O., Echegaray, S., Khuong, A., Hoang, C. D., Shrager, J. B., Jensen, K. C., Berry, G. J., Guo, H. H., Lau, C., Plevritis, S. K., et al. (2017). Predictive radiogenomics modeling of egfr mutation status in lung cancer. *Scientific reports* **7**, 41674.

Guo, W., Li, H., Zhu, Y., Lan, L., Yang, S., Drukker, K., Morris, E. A., Burnside, E. S., Whitman, G. J., Giger, M. L., et al. (2015). Prediction of clinical phenotypes in invasive breast carcinomas from the integration of radiomics and genomics data. *Journal of Medical Imaging* **2**, 041007.

Hänelmann, S., Castelo, R., and Guinney, J. (2013). Gsva: gene set variation analysis for microarray and rna-seq data. *BMC bioinformatics* **14**, 7.

Hu, L. S., Ning, S., Eschbacher, J. M., Baxter, L. C., Gaw, N., Ranjbar, S., Plasencia, J., Dueck, A. C., Peng, S., Smith, K. A., et al. (2017). Radiogenomics to characterize regional genetic heterogeneity in glioblastoma. *Neuro-oncology* **19**, 128–137.

Hurvich, C. M. and Tsai, C. (1990). The impact of model selection on inference in linear regression. *The American Statistician* **44**, 214–217.

Ishida, A., Murray, J., Saito, Y., Kanthou, C., Benzakour, O., Shibuya, M., and Wijelath, E. S. (2001). Expression of vascular endothelial growth factor receptors in smooth muscle cells. *Journal of cellular physiology* **188**, 359–368.

Just, N. (2014). Improving tumour heterogeneity mri assessment with histograms. *British journal of cancer* **111**, 2205.

Karcher, H. (1977). Riemannian center of mass and mollifier smoothing. *Communications on pure and applied mathematics* **30**, 509–541.

Kavanagh, E. and Joseph, B. (2011). The hallmarks of cdkn1c (p57, kip2) in cancer. *Biochimica et Biophysica Acta (BBA)-Reviews on Cancer* **1816**, 50–56.

Kleijn, A., Chen, J. W., Buhrman, J. S., Wojtkiewicz, G. R., Iwamoto, Y., Lamfers, M. L., Stemmer-Rachamimov, A. O., Rabkin, S. D., Weissleder, R., Martuza, R. L., et al. (2011). Distinguishing inflammation from tumor and peritumoral edema by myeloperoxidase magnetic resonance imaging. *Clinical Cancer Research* **17**, 4484–4493.

Kurtek, S. and Bharath, K. (2015). Bayesian sensitivity analysis with the fisher–rao metric. *Biometrika* **102**, 601–616.

Lang, S. (2012). *Fundamentals of differential geometry*, volume 191. Springer Science & Business Media.

Lee, J. D., Sun, D. L., Sun, Y., and Taylor, J. E. (2013). Exact post-selection inference with the lasso. *arXiv:1311.6238 [math, stat]* .

Lee, J. D. and Taylor, J. E. (2014). Exact Post Model Selection Inference for Marginal Screening. In Ghahramani, Z., Welling, M., Cortes, C., Lawrence, N. D., and Weinberger, K. Q., editors, *Advances in Neural Information Processing Systems 27*, pages 136–144. Curran Associates, Inc.

Lee, W., Lim, S., and Kim, Y. (2017). The role of myosin ii in glioma invasion: A mathematical model. *PLoS One* **12**,

Liberzon, A., Subramanian, A., Pinchback, R., Thorvaldsdóttir, H., Tamayo, P., and Mesirov, J. P. (2011). Molecular signatures database (msigdb) 3.0. *Bioinformatics* **27**, 1739–1740.

Mazurowski, M. A. (2015). Radiogenomics: what it is and why it is important. *Journal of the American College of Radiology* **12**, 862–866.

Negrini, S., Gorgoulis, V. G., and Halazonetis, T. D. (2010). Genomic instability—an evolving hallmark of cancer. *Nature reviews Molecular cell biology* **11**, 220–228.

Nicolasjilwan, M., Hu, Y., Yan, C., Meerzaman, D., Holder, C. A., Gutman, D., Jain, R., Colen, R., Rubin, D. L., Zinn, P. O., et al. (2015). Addition of mr imaging features and

genetic biomarkers strengthens glioblastoma survival prediction in tcga patients. *Journal of Neuroradiology* **42**, 212–221.

Panigrahi, S. and Taylor, J. (2019). Approximate selective inference via maximum likelihood. *arXiv preprint:1902.07884* .

Panigrahi, S., Taylor, J., et al. (2018). Scalable methods for bayesian selective inference. *Electronic Journal of Statistics* **12**, 2355–2400.

Panigrahi, S., Taylor, J., and Weinstein, A. (2016). Integrative methods for post-selection inference under convex constraints. *arXiv preprint:1605.08824* .

Panigrahi, S., Zhu, J., and Sabatti, C. (2019). Selection-adjusted inference: an application to confidence intervals for cis-eQTL effect sizes. *Biostatistics* kxz024.

Park, T. and Casella, G. (2008). The bayesian lasso. *Journal of the American Statistical Association* **103**, 681–686.

Röver, L. K., Gevensleben, H., Dietrich, J., Bootz, F., Landsberg, J., Goltz, D., and Dietrich, D. (2018). Pd-1 (pdcd1) promoter methylation is a prognostic factor in patients with diffuse lower-grade gliomas harboring isocitrate dehydrogenase (idh) mutations. *EBioMedicine* **28**, 97–104.

Saha, A., Banerjee, S., Kurtek, S., Narang, S., Lee, J., Rao, G., Martinez, J., Bharath, K., Rao, A. U., and Baladandayuthapani, V. (2016). Demarcate: Density-based magnetic resonance image clustering for assessing tumor heterogeneity in cancer. *NeuroImage: Clinical* **12**, 132–143.

Shinohara, R. T., Sweeney, E. M., Goldsmith, J., Shiee, N., Mateen, F. J., Calabresi, P. A., Jarso, S., Pham, D. L., Reich, D. S., Crainiceanu, C. M., et al. (2014). Statistical normalization techniques for magnetic resonance imaging. *NeuroImage: Clinical* **6**, 9–19.

Song, Y. S., Choi, S. H., Park, C.-K., Yi, K. S., Lee, W. J., Yun, T. J., Kim, T. M., Lee, S.-H., Kim, J.-H., Sohn, C.-H., et al. (2013). True progression versus pseudoprogression in the treatment of glioblastomas: a comparison study of normalized cerebral blood volume

and apparent diffusion coefficient by histogram analysis. *Korean journal of radiology* **14**, 662–672.

Srivastava, A. and Klassen, E. P. (2016). *Functional and shape data analysis*. Springer.

Strickland, M. and Stoll, E. A. (2017). Metabolic reprogramming in glioma. *Frontiers in cell and developmental biology* **5**, 43.

Tian, X., Panigrahi, S., Markovic, J., Bi, N., and Taylor, J. (2016). Selective sampling after solving a convex problem. *arXiv preprint arXiv:1609.05609* .

Tian, X. and Taylor, J. (2018). Selective inference with a randomized response. *The Annals of Statistics* **46**, 679–710.

Tibshirani, R. (1996). Regression shrinkage and selection via the lasso. *Journal of the Royal Statistical Society: Series B* **58**, 267–288.

Tubbs, A. and Nussenzweig, A. (2017). Endogenous dna damage as a source of genomic instability in cancer. *Cell* **168**, 644–656.

Vasaikar, S. V., Straub, P., Wang, J., and Zhang, B. (2017). Linkedomics: analyzing multi-omics data within and across 32 cancer types. *Nucleic acids research* **46**, D956–D963.

Wang, K., Wang, Y., Wang, J., Ma, J., Jiang, T., and Dai, J. (2016). Radiologic features and expression of vascular endothelial growth factor stratify survival outcomes in patients with glioblastoma. *American Journal of Neuroradiology* **37**, 629–635.

Watkins, S., Robel, S., Kimbrough, I. F., Robert, S. M., Ellis-Davies, G., and Sontheimer, H. (2014). Disruption of astrocyte–vascular coupling and the blood–brain barrier by invading glioma cells. *Nature communications* **5**, 1–15.

Yekutieli, D. (2012). Adjusted bayesian inference for selected parameters. *Journal of the Royal Statistical Society: Series B (Statistical Methodology)* **74**, 515–541.

Zhang, Y., Morris, J. S., Aerry, S. N., Rao, A. U., Baladandayuthapani, V., et al. (2019). Radio-ibag: Radiomics-based integrative bayesian analysis of multiplatform genomic data. *The Annals of Applied Statistics* **13**, 1957–1988.

8 Supplementary material

A Proofs of main results

Proof. Proposition 1 Using the following notations for the vectors

$$I_i = \begin{pmatrix} I_{i,1} & \cdots & I_{i,L} \end{pmatrix}, \quad \text{and } \mu(\alpha_{\bar{F}}) = \begin{pmatrix} G_{1;F_1} \alpha_{F_1} & \cdots & G_{i;F_L} \alpha_{F_L} \end{pmatrix},$$

and ignoring the selection-aware nature of our model, we observe that the naive (unconditional) likelihood (Y, I, \mathcal{R}) under (4) and (5) is proportional to

$$\begin{aligned} & \exp(-(Y - G_{\bar{E}}\beta_{\bar{E}})^T(Y - G_{\bar{E}}\beta_{\bar{E}})/2\sigma^2) \cdot \exp(-\mathcal{R}^T\mathcal{R}/2\eta^2) \\ & \times \exp\left(-\sum_{i=1}^n (I_i - \mu(\alpha_{\bar{F}}))^T \Sigma_I^{-1} (I_i - \mu(\alpha_{\bar{F}}))/2\right). \end{aligned} \quad (11)$$

Clearly, we use the independence between the outcome, the intermediary variables and the randomization variable in obtaining the above naive likelihood. Truncating (11) now to the selection event which results in the variable sets

$$\widehat{F}_l(\mathcal{I}_l, G) = F_l, \quad \text{for } 1 \leq l \leq L; \quad \widehat{E}(Y, \mathcal{R}; G_{\bar{F}}) = E$$

yields a joint conditional likelihood:

$$\begin{aligned} & \exp(-(Y - G_{\bar{E}}\beta_{\bar{E}})^T(Y - G_{\bar{E}}\beta_{\bar{E}})/2\sigma^2) \cdot \exp(-\mathcal{R}^T\mathcal{R}/2\eta^2) \\ & \times \exp\left(-\sum_{i=1}^n (I_i - \mu(\alpha_{\bar{F}}))^T \Sigma_I^{-1} (I_i - \mu(\alpha_{\bar{F}}))/2\right) \cdot 1_{\{\widehat{F}_l(\mathcal{I}_l; G) = F_l, 1 \leq l \leq L\}} 1_{\{\widehat{E}(Y, \mathcal{R}; G_{\bar{F}}) = E\}} \end{aligned}$$

(up to a proportionality factor). Marginalizing over the intermediary variables and the randomization variable next gives rise to the normalizing constant

$$\mathbb{P}[\widehat{E}(Y, \mathcal{R}; G_{\bar{F}}) = E \mid \beta_{\bar{E}}] \times \mathbb{P}[\widehat{F}_l(\mathcal{I}_l; G) = F_l \text{ for } l = 1, 2, \dots, L \mid \alpha_{F_1}, \dots, \alpha_{F_L}].$$

Notice, the probability over the intermediary and primary outcome variables decouples, an immediate consequence of the independence we assume between the our primary and intermediary model errors. Lastly, the functions involving exclusively the auxiliary parameters

$$\alpha_{F_1}, \dots, \alpha_{F_L}$$

contribute to constants in our likelihood function in terms of $\beta_{\bar{E}}$. Thus, our conditional likelihood is proportional to

$$\exp(-(\widehat{\beta}_{\bar{E}} - \beta_{\bar{E}})^T \Sigma_{\bar{E}}^{-1} (\widehat{\beta}_{\bar{E}} - \beta_{\bar{E}})/2) \cdot \left\{ \mathbb{P}[\widehat{E}(Y, \mathcal{R}; G_{\bar{F}}) = E \mid \beta_{\bar{E}}] \right\}^{-1}.$$

This matches with the expression in Proposition 1. \square

Before we present the proof for Proposition 2, observe that the stationary equation at the solution of (2) equals

$$\begin{aligned} \left(\mathcal{R}_E^T \quad \mathcal{R}_{E^c}^T \right)^T + \left((G_E^T Y)^T \quad (G_{E^c}^T Y)^T \right)^T - \left((\Lambda_E s_E)^T \quad (\Lambda_{E^c} z)^T \right)^T \\ = \begin{bmatrix} G_E^T G_E + \epsilon I \\ G_{E^c}^T G_E \end{bmatrix} \widehat{\beta}_E^{\text{LASSO}}. \end{aligned} \quad (12)$$

Recall, $\widehat{\beta}_E^{\text{LASSO}}$ denotes the LASSO solution for the E active coordinates. In (12), s_E is a vector of signs of the active LASSO solution and z represents the inactive coordinates of the subgradient vector from the ℓ_1 penalty at the solution. Observe, the active solution, $\widehat{\beta}_E^{\text{LASSO}}$, and the inactive part of the subgradient, z , satisfy the constraints (Lee et al., 2013)

$$\text{sign}(\widehat{\beta}_E^{\text{LASSO}}) = s_E ; \quad \|z\|_\infty < 1. \quad (13)$$

Define:

$$\begin{aligned} U_{s_E} &= \begin{bmatrix} \text{diag}(s_E)(G_E^T G_E + \epsilon I)^{-1} G_E^T G_{\bar{E}} \\ G_{E^c}^T G_{\bar{E}} - G_{E^c}^T G_E (G_E^T G_E + \epsilon I)^{-1} G_E^T G_{\bar{E}} \\ -G_{E^c}^T G_{\bar{E}} + G_{E^c}^T G_E (G_E^T G_E + \epsilon I)^{-1} G_E^T G_{\bar{E}} \end{bmatrix}, \\ V_{s_E} &= \begin{bmatrix} \text{diag}(s_E)(G_E^T G_E + \epsilon I)^{-1} & 0 \\ -G_{E^c}^T G_E (G_E^T G_E + \epsilon I)^{-1} & I \\ G_{E^c}^T G_E (G_E^T G_E + \epsilon I)^{-1} & -I \end{bmatrix}, \quad W_{s_E} = \begin{bmatrix} \text{diag}(s_E)(G_E^T G_E + \epsilon I)^{-1} & 0 \\ -G_{E^c}^T G_E (G_E^T G_E + \epsilon I)^{-1} & I \\ G_{E^c}^T G_E (G_E^T G_E + \epsilon I)^{-1} & -I \end{bmatrix}, \\ t_{s_E} &= (\text{diag}(s_E)(G_E^T G_E + \epsilon I)^{-1} \Lambda_E s_E, -\lambda_{E^c} - G_{E^c}^T G_E (G_E^T G_E + \epsilon I)^{-1} \Lambda_E s_E, \\ &\quad -\lambda_{E^c} + G_{E^c}^T G_E (G_E^T G_E + \epsilon I)^{-1} \Lambda_E s_E)^T, \end{aligned}$$

the matrices characterizing the selection event of interest as a union of polyhedral regions in Proposition 2.

Proof. Proposition 2 To see a proof for Proposition 2, selection of active variables E with signs s_E is equivalent to (13). Using the stationary map (12) for realizations (y, r) and based upon the decomposition $G_{\bar{F}}^T y = G_{\bar{F}}^T G_{\bar{E}} \hat{\beta}_{\bar{E}} + \hat{\beta}^\perp$, we first note that the sign constraints are equivalent to

$$\text{diag}(s_E)(G_E^T G_E + \epsilon I)^{-1}(r_E + G_E^T G_{\bar{E}} \hat{\beta}_{\bar{E}} + \hat{\beta}_E^\perp - \Lambda_E s_E) > 0.$$

Next observe the inactive coordinates of the stationary map yield the equality:

$$r_{E^c} + G_{E^c}^T G_{\bar{E}} \hat{\beta}_{\bar{E}} + \hat{\beta}_{E^c}^\perp - G_{E^c}^T G_E \hat{\beta}_E^{\text{LASSO}} = \Lambda_{E^c} z.$$

Coupled with the equation

$$\hat{\beta}_E^{\text{LASSO}} = (G_E^T G_E + \epsilon I)^{-1}(r_E + G_E^T G_{\bar{E}} \hat{\beta}_{\bar{E}} + \hat{\beta}^\perp - \Lambda_E s_E),$$

the restriction on the ℓ_∞ -norm of inactive subgradient vector z is equivalent to the constraints

$$\begin{aligned} r_{E^c} - G_{E^c}^T G_E (G_E^T G_E + \epsilon I)^{-1} r_E + (G_{E^c}^T G_{\bar{E}} - G_{E^c}^T G_E (G_E^T G_E + \epsilon I)^{-1} G_E^T G_{\bar{E}}) \hat{\beta}_{\bar{E}} \\ + \hat{\beta}_{E^c}^\perp - G_{E^c}^T G_E (G_E^T G_E + \epsilon I)^{-1} \hat{\beta}_E^\perp > -\lambda_{E^c} - G_{E^c}^T G_E (G_E^T G_E + \epsilon I)^{-1} \Lambda_E s_E, \end{aligned}$$

and

$$\begin{aligned} -r_{E^c} + G_{E^c}^T G_E (G_E^T G_E + \epsilon I)^{-1} r_E - (G_{E^c}^T G_{\bar{E}} - G_{E^c}^T G_E (G_E^T G_E + \epsilon I)^{-1} G_E^T G_{\bar{E}}) \hat{\beta}_{\bar{E}} \\ - \hat{\beta}_{E^c}^\perp + G_{E^c}^T G_E (G_E^T G_E + \epsilon I)^{-1} \hat{\beta}_E^\perp > -\lambda_{E^c} + G_{E^c}^T G_E (G_E^T G_E + \epsilon I)^{-1} \Lambda_E s_E. \end{aligned}$$

The union of polytopes now follows from considering all possible signs for the active coefficients, which varies over the set $\{-1, 1\}^{|E|}$. \square

Proof. Theorem 1 To derive an expression for the conditional likelihood, we use a change of measure map from

$$\mathcal{R} \rightarrow (\hat{\beta}_E^{\text{LASSO}}, z),$$

where $\hat{\beta}_E^{\text{LASSO}}$ and z are obtained from the stationary conditions of the randomized LASSO at the solution

$$\begin{aligned} \mathcal{R} &= -G_{\bar{F}}^T G_{\bar{E}} \hat{\beta}_{\bar{E}} + \begin{bmatrix} G_E^T G_E + \epsilon I \\ G_{E^c}^T G_E \end{bmatrix} \hat{\beta}_E^{\text{LASSO}} + (-\hat{\beta}^\perp + ((\Lambda_E s_E)^T, (\Lambda_{E^c} z)^T)^T) \\ &= -G_{\bar{F}}^T G_{\bar{E}} \hat{\beta}_{\bar{E}} + Q \cdot \hat{\beta}_E^{\text{LASSO}} + s(\hat{\beta}^\perp, s_E, z); \end{aligned}$$

$s(\hat{\beta}^\perp, s_E, z_{-E}) = ((\Lambda_E s_E)^T, (\Lambda_{E^c} z)^T)^T - \hat{\beta}^\perp$ and $Q = \begin{bmatrix} G_E^T G_E + \epsilon I \\ G_{E^c}^T G_E \end{bmatrix}$. Noticing that the Jacobian of the above change of variables map dissolves as a constant, the density of $(\hat{\beta}_{\bar{E}}, \hat{\beta}_E^{\text{LASSO}})$ when conditioned upon

$$\{\hat{E} = E, \text{sign}(\hat{\beta}_E^{\text{LASSO}}) = s_E, z = z^{\text{obs}}, \hat{\beta}^\perp = \hat{\beta}^{\perp, \text{obs}}\}$$

is proportional to

$$\begin{aligned} & \exp(-(\hat{\beta}_{\bar{E}} - \beta_{\bar{E}})^T \Sigma_{\bar{E}}^{-1} (\hat{\beta}_{\bar{E}} - \beta_{\bar{E}})/2) \\ & \times \exp\left(-(-G_{\bar{F}}^T G_{\bar{E}} \hat{\beta}_{\bar{E}} + Q \cdot \hat{\beta}_E^{\text{LASSO}} + s(\hat{\beta}^{\perp, \text{obs}}, s_E, z^{\text{obs}}))^T\right. \\ & \quad \left.(-G_{\bar{F}}^T G_{\bar{E}} \hat{\beta}_{\bar{E}} + Q \cdot \hat{\beta}_E^{\text{LASSO}} + s(\hat{\beta}^{\perp, \text{obs}}, s_E, z^{\text{obs}}))/2\eta^2\right) \cdot 1_{\{\text{sign}(\hat{\beta}_E^{\text{LASSO}}) = s_E\}}. \end{aligned}$$

Equivalently, the above density is proportional to

$$\begin{aligned} & \exp(-(\hat{\beta}_{\bar{E}} - \beta_{\bar{E}})^T \Sigma_{\bar{E}}^{-1} (\hat{\beta}_{\bar{E}} - \beta_{\bar{E}})/2) \\ & \times \exp(-(\hat{\beta}_E^{\text{LASSO}} - p(\hat{\beta}_{\bar{E}}))^T Q^T Q (\hat{\beta}_E^{\text{LASSO}} - p(\hat{\beta}_{\bar{E}}))/2\eta^2) \cdot 1_{\{\text{sign}(\hat{\beta}_E^{\text{LASSO}}) = s_E\}}, \end{aligned} \tag{14}$$

where $p(b) = (Q^T Q)^{-1} Q^T \left(G_{\bar{F}}^T G_{\bar{E}} b + \hat{\beta}^{\perp, \text{obs}} - (\Lambda_E s_E, \Lambda_{E^c} z^{\text{obs}})^T \right)$. Letting b represent the variable $\hat{\beta}_{\bar{E}}$ and w represent $\hat{\beta}_E^{\text{LASSO}}$ and integrating over the support of this joint density (14)

$$\{(b, w) : \text{sign}(w) = s_E\},$$

the normalizing constant for this density now equals:

$$\begin{aligned} & \int_{\text{sign}(w)=s_E} (2\pi)^{-|\bar{E}|/2} \cdot \det(\Sigma_{\bar{E}})^{-1/2} \cdot \exp(-(b - \beta_{\bar{E}})^T \Sigma_{\bar{E}}^{-1} (b - \beta_{\bar{E}})/2) \\ & (2\pi)^{-|E|/2} \cdot \det(Q^T Q/\eta^2)^{1/2} \exp(-(w - p(b))^T Q^T Q (w - p(b))/2\eta^2) dw db. \end{aligned}$$

This completes the derivation of our conditional likelihood. \square

Proof. Theorem 2 We begin by computing the Jacobian associated with the transformation of parameters. This is given by the derivative of the map Ψ with respect to $\zeta_{\bar{E}}$. Observe,

$$\begin{aligned} \mathcal{J}(\zeta_{\bar{E}}) &= \partial \Psi(\zeta_{\bar{E}})/\partial \zeta_{\bar{E}} = (I + \eta^{-2} \Sigma_{\bar{E}} P^T Q^T Q P) \\ & \quad - \eta^{-2} \Sigma_{\bar{E}} P^T Q^T Q \cdot \partial(w^*(\zeta_{\bar{E}}))/\partial \zeta_{\bar{E}}. \end{aligned} \tag{15}$$

From the definition of $w^*(\zeta_{\bar{E}})$, we see that it satisfies the estimating equation:

$$\eta^{-2}Q^TQ(w^*(\zeta_{\bar{E}}) - P\zeta_{\bar{E}} - o) + \nabla C_{s_E}(w^*(\zeta_{\bar{E}})) = 0.$$

Taking a derivative with respect to $\zeta_{\bar{E}}$ we have:

$$(\eta^{-2}Q^TQ + \nabla^2 C_{s_E}(w^*(\zeta_{\bar{E}}))) \partial(w^*(\zeta_{\bar{E}})) / \partial \zeta_{\bar{E}} = \eta^{-2}Q^TQP.$$

This implies

$$\partial(w^*(\zeta_{\bar{E}})) / \partial \zeta_{\bar{E}} = (\eta^{-2}Q^TQ + \nabla^2 C_{s_E}(w^*(\zeta_{\bar{E}})))^{-1} \eta^{-2}Q^TQP,$$

and plugged into (15), the Jacobian equals:

$$(I + \eta^{-2}\Sigma_{\bar{E}}P^TQ^TQP) - \eta^{-4}\Sigma_{\bar{E}}P^TQ^TQ(\eta^{-2}Q^TQ + \nabla^2 C_{s_E}(w^*(\zeta_{\bar{E}})))^{-1}Q^TQP.$$

To obtain an expression for the log-posterior, we use the change of measure $\beta_{\bar{E}} \rightarrow \zeta_{\bar{E}}$ formula in (7) to obtain the (transformed) selection-aware posterior

$$\tilde{\pi}(\zeta_{\bar{E}}|\hat{\beta}_{\bar{E}}) = |\mathcal{J}(\zeta_{\bar{E}})| \cdot \pi(\Psi(\zeta_{\bar{E}})|\hat{\beta}_{\bar{E}}).$$

Let b^*, w^* be the optimal solutions for the optimization:

$$\inf_{b,w} \left\{ (b - \Psi(\zeta_{\bar{E}}))^T \Sigma_{\bar{E}}^{-1} (b - \Psi(\zeta_{\bar{E}})) / 2 + (w - p(b))^T Q^T Q (w - p(b)) / 2\eta^2 + C_{s_E}(w) \right\}.$$

Ignoring the normalizing constant, $\log \tilde{\pi}(\zeta_{\bar{E}}|\hat{\beta}_{\bar{E}})$ equals

$$\begin{aligned} & \log |\mathcal{J}(\zeta_{\bar{E}})| + \log \pi(\Psi(\zeta_{\bar{E}})) + \hat{\beta}_{\bar{E}}^T \Sigma_{\bar{E}}^{-1} \Psi(\zeta_{\bar{E}}) - \Psi(\zeta_{\bar{E}})^T \Sigma_{\bar{E}}^{-1} \Psi(\zeta_{\bar{E}}) / 2 \\ & + \inf_{b,w} \left\{ (b - \Psi(\zeta_{\bar{E}}))^T \Sigma_{\bar{E}}^{-1} (b - \Psi(\zeta_{\bar{E}})) / 2 + (w - p(b))^T Q^T Q (w - p(b)) / 2\eta^2 \right. \\ & \quad \left. + C_{s_E}(w) \right\}. \end{aligned} \tag{16}$$

$$= \log |\mathcal{J}(\zeta_{\bar{E}})| + \log \pi(\Psi(\zeta_{\bar{E}})) + \hat{\beta}_{\bar{E}}^T \Sigma_{\bar{E}}^{-1} \Psi(\zeta_{\bar{E}}) \\ - b^{*T} \Sigma_{\bar{E}}^{-1} \Psi(\zeta_{\bar{E}}) + b^{*T} \Sigma_{\bar{E}}^{-1} b^* / 2 + (w^* - p(b^*))^T Q^T Q (w^* - p(b^*)) / 2\eta^2 + C_{s_E}(w^*).$$

Our claim then follows from the estimating equation:

$$\begin{aligned} \Psi(\zeta_{\bar{E}}) &= b^* + \eta^{-2} \Sigma_{\bar{E}} \left(\frac{\partial}{\partial b} w^*(b) \Big|_{b^*} - P \right)^T Q^T Q (w^*(b^*) - p(b^*)) \\ &+ \Sigma_{\bar{E}} \left(\frac{\partial}{\partial b} w^*(b) \Big|_{b^*} \right)^T \nabla C_{s_E}(w^*(b)) \\ &= b^* - \eta^{-2} \Sigma_{\bar{E}} P^T Q^T Q (w^*(b^*) - p(b^*)) \\ &= b^* + \eta^{-2} \Sigma_{\bar{E}} P^T Q^T Q P b^* + \eta^{-2} \Sigma_{\bar{E}} P^T Q^T Q (o - w^*(b^*)). \end{aligned}$$

The second equality relies upon the optimality conditions for w^* :

$$\eta^{-2}Q^TQ(w^*(b^*) - p(b^*)) + \nabla C_{s_E}(w^*(b^*)) = 0.$$

Therefore, from the definition of $\Psi(\zeta_{\bar{E}})$, we deduce $b^* = \zeta_{\bar{E}}$ and using (16) conclude that

$$\log \tilde{\pi}(\zeta_{\bar{E}} | \hat{\beta}_{\bar{E}})$$

equals

$$\begin{aligned} & \log |\mathcal{J}(\zeta_{\bar{E}})| + \log \pi(\Psi(\zeta_{\bar{E}})) + \hat{\beta}_{\bar{E}}^T \Sigma_{\bar{E}}^{-1} \Psi(\zeta_{\bar{E}}) - \zeta_{\bar{E}}^T \Sigma_{\bar{E}}^{-1} \Psi(\zeta_{\bar{E}}) \\ & + \zeta_{\bar{E}}^T \Sigma_{\bar{E}}^{-1} \zeta_{\bar{E}} / 2 + \inf_w \left\{ (w - P\zeta_{\bar{E}} - o)^T Q^T Q (w - P\zeta_{\bar{E}} - o) / 2\eta^2 + C_{s_E}(w) \right\} \end{aligned}$$

up to a constant additive term. \square

Proof. Theorem 3 From the expression of the transformed posterior in Theorem 2, the gradient of $\log \tilde{\pi}(\zeta_{\bar{E}} | \hat{\beta}_{\bar{E}})$ is computed as follows. Observing

$$\eta^{-2}Q^TQ(w^*(\zeta_{\bar{E}}) - P\zeta_{\bar{E}} - o) + \nabla C_{s_E}(w^*(\zeta_{\bar{E}})) = 0,$$

we have

$$\nabla \log \tilde{\pi}(\zeta_{\bar{E}} | \hat{\beta}_{\bar{E}})$$

equals

$$\begin{aligned} & \nabla \log |\det(\mathcal{J}(\zeta_{\bar{E}}))| + (\mathcal{J}(\zeta_{\bar{E}}))^T \cdot \left(\nabla \log \pi(\Psi(\zeta_{\bar{E}})) + \Sigma_{\bar{E}}^{-1} \hat{\beta}_{\bar{E}} - \Sigma_{\bar{E}}^{-1} \zeta_{\bar{E}} \right) \\ & - \Sigma_{\bar{E}}^{-1} \cdot \Psi(\zeta_{\bar{E}}) + \Sigma_{\bar{E}}^{-1} \zeta_{\bar{E}} - P^T Q^T Q (w^*(\zeta_{\bar{E}}) - P \cdot \zeta_{\bar{E}} - o) / \eta^2 \\ & = \nabla \log |\det(\mathcal{J}(\zeta_{\bar{E}}))| + (\mathcal{J}(\zeta_{\bar{E}}))^T \left(\nabla \log \pi(\Psi(\zeta_{\bar{E}})) + \Sigma_{\bar{E}}^{-1} \hat{\beta}_{\bar{E}} - \Sigma_{\bar{E}}^{-1} \zeta_{\bar{E}} \right). \end{aligned}$$

The last equality follows from the definition of the reparameterization map (8).

Recall,

$$\begin{aligned} \mathcal{J}(\zeta_{\bar{E}}) &= (I + \eta^{-2} \Sigma_{\bar{E}} P^T Q^T Q P) \\ & - \eta^{-4} \Sigma_{\bar{E}} P^T Q^T Q (\eta^{-2} Q^T Q + \nabla^2 C_{s_E}(w^*(\zeta_{\bar{E}})))^{-1} Q^T Q P. \end{aligned}$$

Let the j -th column of the matrix

$$\partial(w^*(\zeta_{\bar{E}})) / \partial \zeta_{\bar{E}} = (\eta^{-2} Q^T Q + \nabla^2 C_{s_E}(w^*(\zeta_{\bar{E}})))^{-1} \eta^{-2} Q^T Q P$$

be \mathcal{J}_j . Before computing the derivative, we make the observation that this matrix is non-singular. This follows directly by representing the Jacobian matrix as follows:

$$\begin{aligned} & \Sigma_{\bar{E}} \cdot \left(\Sigma_{\bar{E}}^{-1} + \eta^{-2} P^T Q^T \left[I - \eta^{-2} Q (\nabla^2 C_{s_E})^{-1/2} (\eta^{-2} (\nabla^2 C_{s_E})^{-1/2} Q^T Q \right. \right. \\ & \quad \left. \left. (\nabla^2 C_{s_E})^{-1/2} + I \right)^{-1} (\nabla^2 C_{s_E})^{-1/2} Q^T \right] Q P \right) \\ &= \Sigma_{\bar{E}} \cdot \left(\Sigma_{\bar{E}}^{-1} + \eta^{-2} P^T Q^T (I + \eta^{-2} Q (\nabla^2 C_{s_E})^{-1} Q^T)^{-1} Q P \right). \end{aligned}$$

The proof is complete by calculating $\nabla \log |\det(\mathcal{J}(\zeta_{\bar{E}}))|$, whose j -th coordinate equals:

$$\begin{aligned} & \text{Trace} \left(-\eta^{-4} \mathcal{J}^{-1}(\zeta_{\bar{E}}) \Sigma_{\bar{E}} P^T Q^T Q \cdot \frac{\partial}{\partial \zeta_{j, \bar{E}}} (N^{-1}) Q^T Q P \right) \\ &= \text{Trace} \left(\eta^{-4} \mathcal{J}^{-1}(\zeta_{\bar{E}}) \Sigma_{\bar{E}} P^T Q^T Q N^{-1} \left(\frac{\partial}{\partial \zeta_{j, \bar{E}}} (N(\zeta_{\bar{E}})) \right) \right. \\ & \quad \left. N^{-1} Q^T Q P \right) \\ &= \text{Trace} \left(\eta^{-4} \mathcal{J}^{-1}(\zeta_{\bar{E}}) \Sigma_{\bar{E}} P^T Q^T Q N^{-1} \left(\tilde{C}_{s_E}(w^*(\zeta_{\bar{E}})) \cdot \text{diag}(\mathcal{J}_j) \right) \right. \\ & \quad \left. N^{-1} Q^T Q P \right), \end{aligned}$$

where the l -th diagonal entry of $\tilde{C}_{s_E}(w^*(\zeta_{\bar{E}}))$ equals $\nabla^3 B_l(w^*)$ and $\text{diag}(\mathcal{J}_j)$ is a diagonal matrix with the vector \mathcal{J}_j along the diagonal. \square

B Working version of selection-aware posterior

We give details for the working selection-aware posterior (7) below. Specifically, we use a Laplace approximation to $I(\beta_{\bar{E}})$ leading to an approximate expression for the (log-) likelihood:

$$\begin{aligned} & -(\hat{\beta}_{\bar{E}} - \beta_{\bar{E}})^T \Sigma_{\bar{E}}^{-1} (\hat{\beta}_{\bar{E}} - \beta_{\bar{E}})/2 \\ & + \inf_{b, w} \left\{ (b - \beta_{\bar{E}})^T \Sigma_{\bar{E}}^{-1} (b - \beta_{\bar{E}})/2 + (w - p(b))^T Q^T Q (w - p(b))/2\eta^2 + C_{s_E}(w) \right\}; \end{aligned}$$

where

$$C_{s_E}(w) = \sum_{j=1}^{|E|} \log(1 + (Q^T Q)_{j,j}^{1/2} \cdot (\eta s_{E;j} w_j)^{-1}) = \sum_{j=1}^{|E|} B_j(w_j), \quad (17)$$

$(Q^T Q)_{j,j}^{1/2}$ is the j -th diagonal entry of $(Q^T Q)^{1/2}$; $s_{E;j}$ is the j -th entry of the sign vector s_E . Appending the working expression for our (log-) likelihood to a prior finally gives rise to a tractable version for the selection-aware posterior in (7). For the sake of completeness, we

include the finite-sample motivation behind the approximation as an upper bound on the selection probability.

Proposition 3. *Consider the modeling assumptions 4 and 5. For an arbitrary convex, compact region K , we have the following upper bound*

$$\begin{aligned} \mathbb{P} \left[(\widehat{\beta}_{\bar{E}}, \widehat{\beta}_E^{\text{LASSO}}) \in K \mid \beta_{\bar{E}} \right] &\leq (2\pi)^{-|\bar{E}|/2} \cdot \det(\Sigma_{\bar{E}})^{-1/2} \\ &\times \exp \left(- \inf_{(b,w) \in K} \left\{ (b - \beta_{\bar{E}})^T \Sigma_{\bar{E}}^{-1} (b - \beta_{\bar{E}})/2 + (w - p(b))^T Q^T Q (w - p(b))/2\eta^2 \right\} \right), \end{aligned}$$

where $p(\cdot)$ and Q are defined in Theorem 1.

Proof. Denoting the MGF of the random variables $(\widehat{\beta}_{\bar{E}}, \widehat{\beta}_E^{\text{LASSO}})$ at (η_1, η_2) as $\Lambda(\eta_1, \eta_2)$ with respect to their density before selection (see Theorem 1)

$$\begin{aligned} (2\pi)^{-|\bar{E}|/2} \cdot \det(\Sigma_{\bar{E}})^{-1/2} \cdot \exp(-(\widehat{\beta}_{\bar{E}} - \beta_{\bar{E}})^T \Sigma_{\bar{E}}^{-1} (\widehat{\beta}_{\bar{E}} - \beta_{\bar{E}})/2) \\ \times \exp(-(\widehat{\beta}_E^{\text{LASSO}} - p(\widehat{\beta}_{\bar{E}}))^T Q^T Q (\widehat{\beta}_E^{\text{LASSO}} - p(\widehat{\beta}_{\bar{E}}))/2\eta^2), \end{aligned}$$

observe that:

$$\begin{aligned} \log \mathbb{P} \left[(\widehat{\beta}_{\bar{E}}, \widehat{\beta}_E^{\text{LASSO}}) \in K \mid \beta_{\bar{E}} \right] \\ \leq \log \mathbb{E} \left[\exp \left(\eta_1^T \widehat{\beta}_{\bar{E}} + \eta_2^T \widehat{\beta}_E^{\text{LASSO}} - \inf_{(b,w) \in K} \{ \eta_1^T b + \eta_2^T w \} \right) \mid \beta_{\bar{E}} \right] \\ = \sup_{(b,w) \in K} -\eta_1^T b - \eta_2^T w + \log \Lambda(\eta_1, \eta_2). \end{aligned}$$

Since the above inequality holds for any η_1, η_2 , optimizing over the parameters η_1, η_2 and using a minimax equality for a convex and compact subset K yields the following bound on the log-selection probability (ignoring constants):

$$\begin{aligned} &- \sup_{\eta_1, \eta_2} \inf_{(b,w) \in K} \left\{ \eta_1^T b + \eta_2^T w - \log \Lambda(\eta_1, \eta_2) \right\} \\ &= - \inf_{(b,w) \in K} \sup_{\eta_1, \eta_2} \left\{ \eta_1^T b + \eta_2^T w - \log \Lambda(\eta_1, \eta_2) \right\} \\ &= - \inf_{(b,w) \in K} \left\{ (b - \beta_{\bar{E}})^T \Sigma_{\bar{E}}^{-1} (b - \beta_{\bar{E}})/2 \right. \\ &\quad \left. + (w - p(b))^T Q^T Q (w - p(b))/2\eta^2 \right\}. \end{aligned}$$

□

The selection probability in Theorem 1 is calculated over the region $\{(b, w) : \text{sign}(w) = s_E\}$, which is convex but not compact. Yet, the approximate posterior obtained by appending a prior to the conditional likelihood and plugging in the bound in Proposition 3 works well under the assumption that we can consider a large enough compact subset K' of the region: $\{(b, w) : \text{sign}(w) = s_E\}$ for all $\beta_{\bar{E}}$ in a bounded set of probability close to 1 under $\pi(\cdot)$. Rigorous asymptotic justification of the approximate selection-aware posterior is based on consistency guarantees aligned along the moderate deviations scale in (Panigrahi and Taylor, 2019); we refer interested readers to this previous work for more details on this topic.

C Radiogenomic feature construction: details

Below, we include details on the construction of gene pathway scores and radiomic measurements which we use for radiogenomic modeling and inference.

C.1 Pathway scores

Pathway based methods provide significant benefits by offering interpretability, as gene functions are exerted collectively and may vary based on several factors such as genetic modification, disease state, or environmental stimuli. Using pathways provides an intuitive way and a stable context for assessing the biological activity (Hänzelmann et al., 2013). Pathway scores are computed using the gene-set variation analysis (GSVA), which estimates a value per sample for the variation of pathway activity within an entire gene expression set, using a non-parametric and unsupervised approach (Hänzelmann et al., 2013). In other words, a pathway score assesses the relative variability of gene expression of the genes in the pathway as compared to expression of genes not in the pathway. We give a brief overview of the analytical procedure for GSVA next.

Let Z be the $p \times n$ matrix of normalized gene expression values corresponding to p genes and n samples ($p \gg n$). Let $G = \{g_1, \dots, g_m\}$ represent a collection of pathways (also referred to as gene-sets). Each pathway g_k is defined as $g_k \subset \{1, \dots, p\}$ with $|g_k|$ denoting its cardinality. Let the expression profile for the gene i be given as $z_i = (z_{i1}, \dots, z_{in})$.

Firstly, in the context of the sample population distribution GSVA evaluates whether a

gene i is highly or lowly expressed in the sample j . To compare distinct expression profiles on the same scale, an expression-level statistic is computed. A non-parametric kernel estimation of the cumulative density function is performed for each z_i using a Gaussian kernel, that is, we compute $\hat{F}_{s_i}(z_{ij}) = \frac{1}{n} \sum_{r=1}^n \Phi(\frac{z_{ij} - z_{ir}}{s_i})$. Here s_i is the gene-specific bandwidth parameter controlling the resolution of the kernel estimation. These statistics $\hat{F}_{s_i}(z_{ij})$ are converted to ranks $r_{(i)j}$ for each sample j . The ranks $r_{(i)j}$ are normalized further as $t_{ij} = |\frac{p}{2} - r_{(i)j}|$ so that the tails of the rank distribution are up-weighted while computing the enrichment score. The normalized ranks t_{ij} are used to compute a Kolmogorov-Smirnov (KS) type random walk statistic for $l = 1, \dots, p$ as

$$\eta_{jk}(l) = \frac{\sum_{i=1}^l |t_{ij}|^\tau I(u_{(i)} \in g_k)}{\sum_{i=1}^p |t_{ij}|^\tau I(u_{(i)} \in g_k)} - \frac{\sum_{i=1}^l I(u_{(i)} \in g_k)}{p - |g_k|}.$$

Here $I(u_{(i)} \in g_k)$ is an indicator taking the value 1 if the gene corresponding to the rank i expression level statistic belongs to the pathway g_k and τ is the parameter describing the weight of the tail. By identifying if the genes in a pathway are more likely to belong to either tail of the rank distribution, the statistic $\eta_{jk}(l)$ produces a distribution over the genes. The enrichment score for the pathway g_k and the sample j is constructed by converting the corresponding KS-like statistic as $S_{jk} = \max_l(0, \eta_{jk}(l)) - \min_l(0, \eta_{jk}(l))$. S_{jk} has a clear biological interpretation as it emphasizes genes in pathways that are concordantly activated in one direction only, which are either over-expressed or under-expressed relative to the overall population (Hänelmann et al., 2013). Low enrichment is shown for pathways containing genes strongly acting in both directions. The computations are performed using the GSVA package in R obtained from the Bioconductor package (Gentleman et al., 2004) under the default settings for the choice of parameters.

D MRI scans and radiomic phenotypes

We consider four types of MRI sequences which include (i) native (T1), (ii) post-contrast T1-weighted (T1Gd), (iii) T2-weighted (T2), and (iv) T2 fluid attenuated inversion recovery (FLAIR) volumes. Each of these sequences display different types of tissues with varying

contrasts based on the tissue characteristics. Note that the whole brain MRI scans are three dimensional objects and have an array structure. In Figure 6, we show an axial slice from the MRI scan of a LGG subject corresponding to all four imaging sequences with the segmented tumor region indicated by a (red) boundary overlaid on those images. This tumor region is further classified into sub-regions (NC, ED and ET) by GLISTRboost as shown in Figure 6.

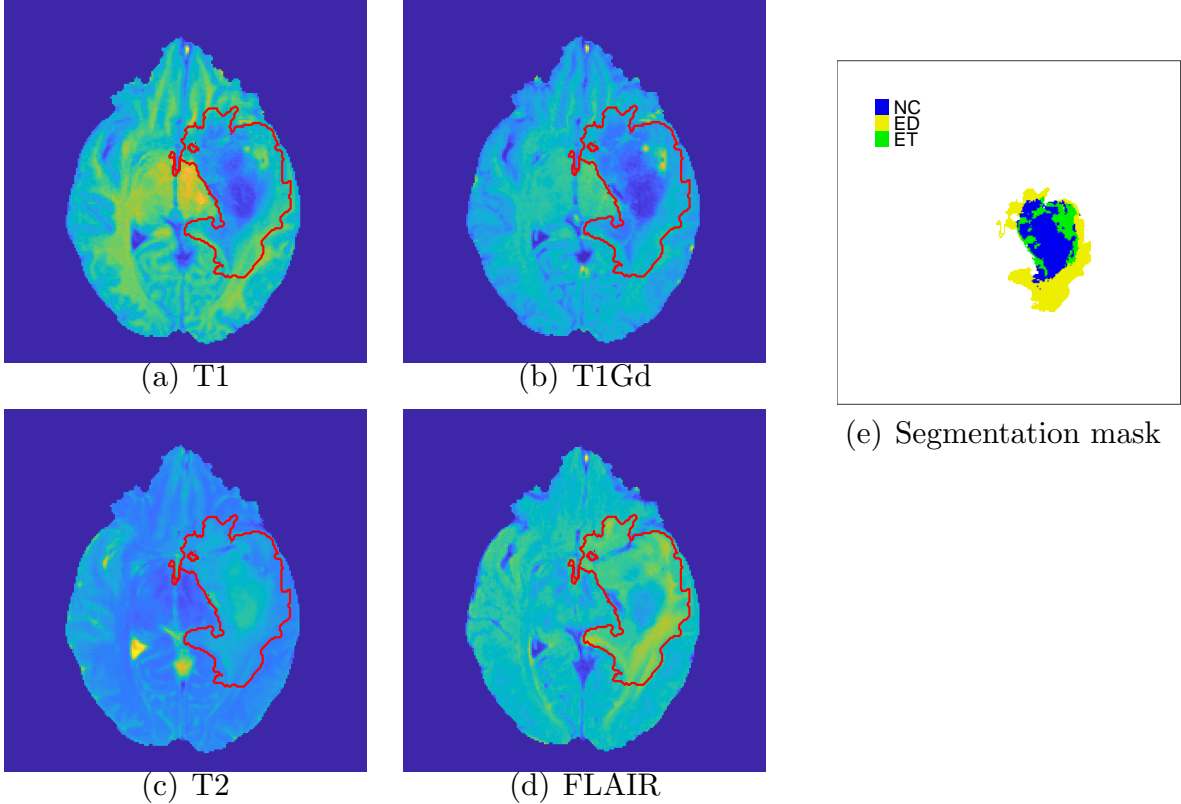


Figure 6: An axial slice of a brain MRI from four modalities: T1, T1Gd, T2 and FLAIR for a LGG subject. The segmented tumor region is shown with an (red) overlaid boundary. Segmentation mask indicates the necrotic and non-enhancing tumor core (NC), the peritumoral edema (ED) and the enhancing tumor (ET) regions.

Voxel-level features are usually extracted to provide additional insight into the tumor physiology, and have been studied in the context of the progression (or regression) of tumors. Summary statistics such as percentiles, quartiles, skewness, kurtosis etc., are evaluated to represent a region of interest and are used as features/covariates in downstream analysis (Baek et al., 2012; Just, 2014; Song et al., 2013). However, some of their drawbacks include the subjectivity in the choice of number and location of summary features, and limitations

in terms of capturing entire information from the histogram of intensity values. To address this, we consider the smoothed density arising from the voxel-level intensity histogram which incorporates granular characteristics of tumor heterogeneity (Saha et al., 2016). The variability in these intensity histograms across the subjects is captured through the scores from a principal component analysis on the space of density functions using a Riemannian-geometric framework. In other words, these principal component scores obtained from the density functions act as the radiomic phenotypes which capture the heterogeneity in the tumor voxels from the MRI scans. We include these details in Sections D and D.1.

D.1 Principal Component Scores

Next, we discuss the construction of the principal component scores when we have probability density functions (pdfs) as data objects corresponding to n samples. Without loss of generality, let us consider densities on $[0, 1]$ and let \mathcal{F} denote the Banach manifold of such pdfs defined as $\mathcal{F} = \{f : [0, 1] \rightarrow \mathbb{R}_+ \mid \int_0^1 f(x)dx = 1\}$. A non-parametric Fisher-Rao Riemannian metric which is invariant to reparameterizations can be defined, however it is computationally challenging to compute the geodesic paths and distances using this metric (Srivastava and Klassen, 2016).

An equivalent representation of the space \mathcal{F} via the square-root transformation (SRT) representation (Bhattacharyya, 1943) simplifies computations. The SRT is defined as a function $h = +\sqrt{f}$ (we omit the $+$ sign hereafter for notational convenience). Also, the inverse mapping is unique and is simply given by $f = h^2$ (Kurtek and Bharath, 2015). Space of SRTs is given by $\mathcal{H} = \{h : [0, 1] \rightarrow \mathbb{R}^+ \mid \int_0^1 h(x)^2dx = 1\}$ and represents the positive orthant of a unit Hilbert sphere (Lang, 2012). The \mathbb{L}^2 Riemannian metric on \mathcal{H} can be defined as $\langle\langle \delta h_1, \delta h_2 \rangle\rangle = \int_0^1 \delta h_1(t)\delta h_2(t)dt$, where $\delta h_1, \delta h_2 \in T_h(\mathcal{H})$ and $T_h(\mathcal{H}) = \{\delta h : [0, 1] \rightarrow \mathbb{R} \mid \int_0^1 h(x)\delta h(x)dx = 0\}$. The geodesic paths and lengths can now be analytically computed due to the Riemannian geometry of \mathcal{H} equipped with the \mathbb{L}^2 metric. The geodesic distance between $h_1, h_2 \in \mathcal{H}$ is simply given by $d(h_1, h_2) = \theta = \cos^{-1} \left(\int_0^1 h_1(x)h_2(x)dx \right)$.

The geometry of the space of SRTs can be used to define an average (or mean) density corresponding to a sample of density functions. This allows us to efficiently summarize and visualize a sample of densities. The average pdf can be computed using a generalized

version of mean on a metric space called the *Karcher* mean (Karcher, 1977). Suppose we have n pdfs f_1, \dots, f_n and the corresponding SRTs as h_1, \dots, h_n . The sample Karcher mean \bar{h} on \mathcal{H} is defined as the minimizer of the Karcher variance $\rho(\bar{h}) = \sum_{i=1}^n d(h_i, \bar{h})_{\mathbb{L}^2}^2$, that is, $\bar{h} = \operatorname{argmin}_{h \in \mathcal{H}} d(h_i, \bar{h})_{\mathbb{L}^2}^2$. Algorithm 1 presents a gradient-based approach to compute the Karcher mean on \mathcal{H} (Dryden and Mardia, 1998).

Algorithm 1 Sample Karcher mean of densities

```

1:  $\bar{h}_0$  (initial estimate for the Karcher mean)  $\leftarrow$  any one of the densities in the sample OR
   the extrinsic average. Set  $j \leftarrow 0$  and  $\epsilon_1, \epsilon_2 > 0$  be small.
2: For  $i = 1, \dots, n$  compute  $u_i = \exp_{\bar{h}_j}^{-1}(h_i)$ .
3: Compute the average direction in the tangent space  $\bar{u} = \frac{1}{n} \sum_{i=1}^n u_i$ .
4: if  $\|\bar{u}\|_{L^2} < \epsilon_1$  then
5:   return  $\bar{h}_j$  as the Karcher mean.
6: else
7:    $\bar{h}_{j+1} = \exp_{\bar{h}_j}(\epsilon_2 \bar{u})$ .
8:   Set  $j \leftarrow j + 1$ .
9:   Return to step 2.

```

Note that the Karcher mean of the sample pdfs is an intrinsic average that is computed directly on \mathcal{H} (or equivalently \mathcal{F}). Hence we have a mean which is an actual pdf (Karcher mean) and a distance function. Here the inverse exponential map, denoted by $\exp_{h_1}^{-1} : \mathcal{H} \mapsto T_{h_1}(\mathcal{H})$, is given by $\exp_{h_1}^{-1}(h_2) = (\theta / \sin(\theta))(h_2 - h_1 \cos(\theta))$. The exponential map at a point $h_1 \in \mathcal{H}$, denoted by $\exp : T_{h_1}(\mathcal{H}) \mapsto \mathcal{H}$, is defined as $\exp_{h_1}(\delta h) = \cos(\|\delta h\|)h_1 + \sin(\|\delta h\|)(\delta h / \|\delta h\|)$, where $\|\delta h\| = (\int_0^1 \delta h(x)^2 dx)^{1/2}$.

Under the standard settings, visualizing the space of pdfs intuitively is not straight forward. Principal component analysis (PCA) is an effective method to explore the variability in the pdfs through their primary modes of variation in the data. Note that the tangent space is a vector space (Euclidean), hence PCA can be implemented, as in standard problems. Algorithm 2 describes the computation of PCA on the space generated by the pdfs f_1, \dots, f_n and the corresponding SRTs h_1, \dots, h_n .

Note that the first r columns of U (denoted as $\tilde{U} \in \mathbb{R}^{m \times r}$) span the r -dimensional

Algorithm 2 PCA on \mathcal{P}

- 1: Compute the Karcher mean of h_1, \dots, h_n as \bar{h} .
- 2: **for** $i = 1, \dots, n$ **do**
- 3: Compute projections ($v_i = \exp_{\bar{h}}^{-1}(h_i)$) of h_i onto $T_{\bar{h}}(\mathcal{H})$.
- 4: Evaluate sample covariance matrix $K = \frac{1}{n-1} \sum_{i=1}^n v_i v_i^\top \in \mathbb{R}^{m \times m}$.
- 5: Compute the SVD of $K = U \Sigma U^\top$.

principal subspace. We can compute the principal coefficients as $X = V\tilde{U}$, where $V^\top = [v_1 \ v_2 \ \dots \ v_n] \in \mathbb{R}^{m \times n}$. These principal coefficients X (principal component scores) act as Euclidean coordinates corresponding to densities f_i and can be used as predictors for downstream modeling.

In Figure 7, we represent the workflow to construct the principal component scores using the tumor intensity values for the T1 MRI sequence. The same workflow is followed for the other three MRI sequences to compute the principal component scores. The number of principal components to include could be chosen using a threshold on the percent variance explained.

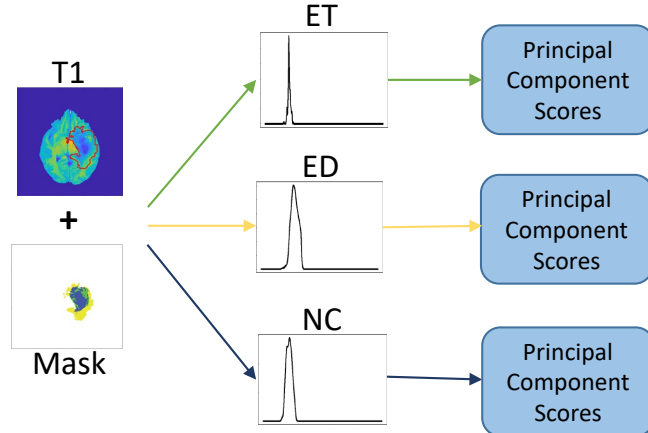


Figure 7: Workflow to obtain the principal component scores from the tumor sub-regions (ND, ET, and ED) in the T1 MRI scan.